A numerical investigation of the oceanic general circulation

By KIRK BRYAN and MICHAEL D. COX, *Geophysical Fluid Dynamics Laboratory, Environmental Science Services Administration, Washington, D.C.*

(Manuscript received October 5, 1965)

ABSTRACT

An ocean basin of uniform depth is considered. It is bounded laterally by two meridians. Temperature and wind stress are specified as functions of latitude at the upper surface. The physical model is similar to that used in previous models of the oceanic thermocline, except that the momentum equations of the horizontal velocity components are retained in nearly complete form. Solutions are obtained by the direct numerical integration of a corresponding initial value problem using an electronic computer. Dimensional analysis indicates that the system depends on 5 basic parameters. The geophysically significant range of these parameters is investigated in 8 numerical experiments.

Computations with and without wind stress show the interaction of the thermohaline and the wind-driven components of the large scale circulation. Without wind a single large anticyclonic gyre extends over the entire surface of the basin. There is a shallow western boundary current, extending to high latitudes, and a vertically uniform southward drift in the interior from the surface down to the base of the thermocline. A sluggish cyclonic gyre exists below the thermocline. The addition of a wind stress pattern corresponding to a maximum in the westerlies at 45° N leads to the formation of an additional cyclonic gyre in subarctic latitudes. In spite of the simplified boundary conditions the solutions with wind stress reproduce many details of the observed density structure in the North Atlantic, particularly in the subtropical gyre.

A more quantitative comparison with North Atlantic data indicates that a choice of the vertical diffusion coefficient, $\varkappa$, to be 1 cm^2/s gives an approximate fit to the thermocline depth and estimates of the total poleward transport of heat. The corresponding renewal time for deep water, however, is considerably less than that indicated by C^{14} data.

1. Introduction

Due to difficulties of measurement very little is known about the velocity field in the ocean and its temporal fluctuations. On the other hand, extensive measurements of the density structure have been made. Data indicate that the density structure is remarkably conservative in its large scale features. For example, hydrographic sections made by the *Meteor* expedition in the Atlantic compare very closely to sections made several decades later by vessels of the Woods Hole Oceanographic Institution during the IGY. This means that a large body of data collected at widely separated points in time may be combined to give a fairly comprehensive picture of the mass structure in the more frequented parts of the world ocean. Examples of this data are the three east-west density sections based on IGY data shown in Fig. 1.

Recently some success has been achieved in constructing theories of the oceanic thermocline which predict major features of the observed density structure. Notable contributions to this subject have been made by Lineykin (1955, 1962), Robinson & Stommel (1959), Welander (1959) and Stommel & Webster (1962). This direction of research has one very important advantage relative to the dynamic investigations of wind-driven ocean circulation which predict the field of total mass transport (see Stommel 1958, 1965, for a review). Since only a few acceptable direct measurements of total mass transport in the ocean are available, it is impossible to really verify the wind-driven ocean theories in the same way in which the

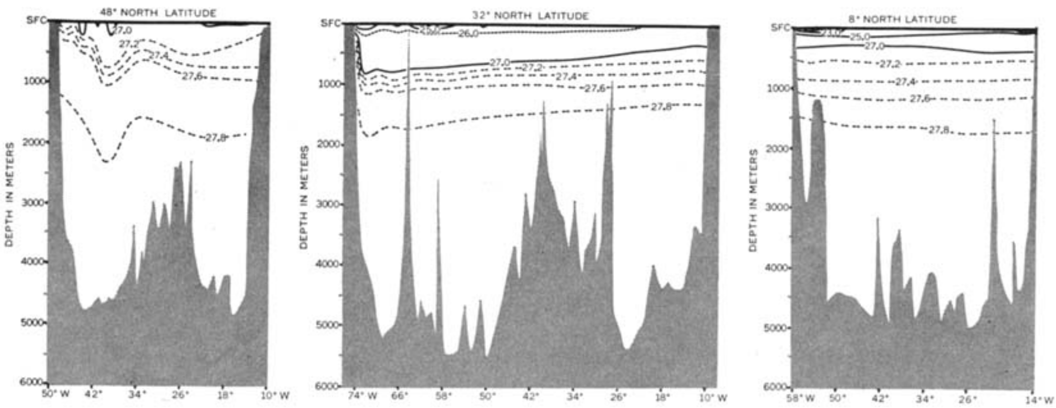

Fig. 1*a* Fig. 1*b* Fig. 1*c*

FIG. 1. East-west sections of σ_t for the Atlantic Ocean. σ_t is equal to $(\varrho - 1.0) \times 10^3$, where ϱ is the density referred to surface pressure. The σ_t values are based on calculations by the National Oceanographic Data Center, Washington, D.C., U.S.A., based on IGY data (FUGLISTER, 1960).

thermocline solutions can be verified by comparison with actual temperature and salinity data.

The thermocline investigations have developed steady-state solutions for the three-dimensional velocity and temperature structure based on physical models of the ocean which are appropriate to the subtropics away from strong boundary currents. Only part of an ocean basin is considered explicitly. A weakness of the theory is that the similarity solutions on which it is based may specify a different interaction between the particular region of the ocean under consideration and other parts of the ocean than would naturally occur.

The present study is an attempt to overcome this difficulty by seeking solutions of a more general model for the entire region of an ocean basin. In order to do this the analytic approach of previous thermocline studies has been abandoned, and steady state solutions have been sought by a direct numerical solution of an initial value problem. Pioneering work along these lines has already been carried out for a geostrophic baroclinic model by SARKISYAN (1962), and GORMATYUK & SARKISYAN (1965). The general approach in the present study is also similar to a numerical study of the atmospheric general circulation using the primitive hydrodynamic equations carried out by SMAGORINSKY (1963). Since small, but significant departures from geostrophy may be expected in strong currents adjacent to the western boundary, the mathematical model includes the momentum equations for the horizontal components of velocity in nearly complete form. The vertical diffusion coefficient is made a simple function of static stability. In regions of stable stratification the vertical diffusion coefficient is a constant as in the ROBINSON & STOMMEL (1959) thermocline model. In areas of unstable stratification the vertical diffusion for heat is set equal to infinity in order to model the free convection regimes which will occur due to cooling at the surface in subarctic and arctic regions.

The numerical method, although very powerful in other respects, is limited in that only part of the spectrum of all possible horizontal scales can be resolved. The effect of lateral motions too small to be included explicitly must be taken into account by a "turbulent viscosity" hypothesis. The new parameter introduced may be formulated as an effective Reynolds number. Since no physical basis exists on the basis of oceanographic observations to assign any fixed value to such a parameter, calculations are done for different Reynolds numbers and the results extrapolated over as wide a range as possible. The near linear solutions for low Reynolds number are most accessible to a numerical calculation with a numerical net with coarse resolution, and are the easiest to interpret. Such calculations are a valuable reference for understanding the more complicated nonlinear regimes at higher Reynolds number.

The numerical method is tested by comparison with the similarity theory of ROBINSON & WELANDER (1963). The results are given in Appendix A.

2. Equations of the model

The density anomaly of sea water is due to the distribution of both salinity and temperature. Source or sink regions for salinity at the ocean surface coincide with areas in which evaporation exceeds precipitation, or vice versa. With the important exception of the equatorial rain belt, the ocean surface at low latitudes is both a source of heat and salinity. On the other hand, cooling and an excess of precipitation make the ocean surface in subarctic areas a sink of both heat and salinity. To simplify the formulation of the present study it will be assumed that the boundary conditions of temperature and salinity are independent of longitude and have the same dependence on latiude. If second and higher order terms are neglected, an equation of state is

$$\varrho = \varrho_0[1 - \alpha(T - T_0) + \sigma(S - S_0)],$$

where T, S and ϱ are temperature, salinity, and density, respectively. α and σ are expansion coefficients. In the case of a linear equation of state an apparent temperature, ϑ, may be defined (FOFONOFF, 1962),

$$\vartheta = T - T_0 - \frac{\sigma}{\alpha}(S - S_0).$$

As a matter of convenience the word temperature is used synonymously with the apparent temperature in the following sections.

The equations of motion are written for a mercator projection in a rotating frame of reference with the following assumptions: (a) hydrostatic balance, (b) variations in density neglected except where they appear as a coefficient of g (the gravitational acceleration), (c) viscosity and conductivity are replaced by new terms representing the diffusion of momentum and heat by smaller scale, transient disturbances.

Let
$$m = \sec \varphi,$$
$$n = \sin \varphi,$$

where φ is the latitude. If λ is the longitude and a is the radius of the globe, x and y coordinates are defined as

$$dx = a d\lambda,$$

$$dy = amd\varphi.$$

Let μ be some scalar quantity and

$$D\mu = \mu_T + mu\mu_x + mv\mu_y + w\mu_z,$$

where u, v and w are the velocity components in the x, y and z-directions. The simplified equation of state used in these computations is simply,

$$\varrho' = \varrho_0(1 - \alpha\vartheta').$$

With this notation the equations of motion and continuity are:

$$Du' - n(2\Omega + u'm/a)v' = -m(p'/\varrho_0)_x + F^x, \quad (2.1)$$

$$Dv' + n(2\Omega + u'm/a)u' = -m(p'/\varrho_0)_y + F^y, \quad (2.2)$$

$$g\varrho'/\varrho_0 = -(p'/\varrho_0)_z, \quad (2.3)$$

$$m^2[(u'/m)_x + (v'/m)_y] = -w'_z. \quad (2.4)$$

In anticipation of scaling, all real variables are denoted by a prime. Primes on subscripts will be understood.

The conservation equation for the apparent temperature is

$$D\vartheta' = Q. \quad (2.5)$$

F^x, F^y and Q represent the assumed contribution of scales of motion less than the numerical grid to the exchange of heat and momentum.

$$F^x = \varkappa u'_{zz} + A_M m^2 \nabla^2 u', \quad (2.6)$$

$$F^y = \varkappa v'_{zz} + A_M m^2 \nabla^2 v' \quad (2.7)$$

and
$$Q = \frac{\varkappa}{\delta}\vartheta'_{zz} + A_H m^2 \nabla^2 \vartheta', \quad (2.8)$$

where
$$\nabla^2(\ ) = (\ )_{xx} + (\ )_{yy}. \quad (2.9)$$

This formulation allows for a nonisotropic mixing with a horizontal mixing length which may be very different from that in the vertical. Larger scales of turbulent motion in the ocean have a tendency to take place along isentropic surfaces, rather than strictly horizontal sur-

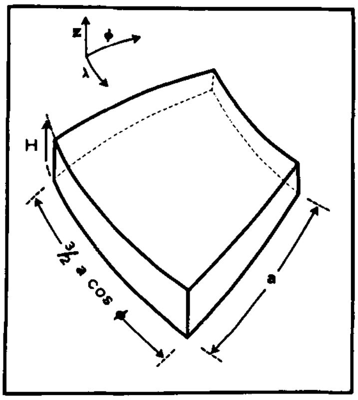

Fig. 2a

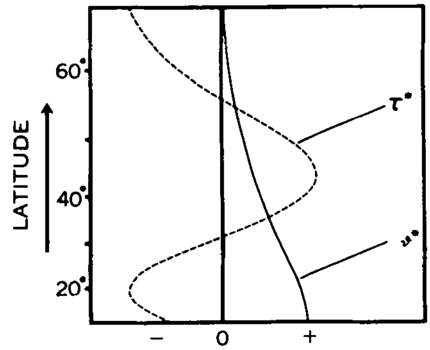

Fig. 2b

FIG. 2. (a) Sketch of the basin, (b) The temperature specified at the surface, ϑ^*, and the x-component of the surface wind stress.

faces. It is therefore reasonable that the lateral mixing of the apparent temperature, A_H, should be less than the lateral mixing of momentum given by A_M.

δ in equation (2.8) is

$$\delta = \begin{matrix} 0 & \vartheta_z' < 0 \\ 1 & \vartheta_z' > 0 \end{matrix} \qquad (2.10)$$

indicating that the vertical mixing of temperature is a constant for stable stratification, but effectively infinite for unstable cases.

The calculations are carried out for a basin of plantary scale bounded laterally by two meridians and two latitude circles. A sketch of the basin is shown in Fig. 2a. For convenience in description the basin will be thought of as in the northern hemisphere, so that north and south indicate the direction toward the pole and toward the equator, respectively. The south wall is placed at 11.5° N. Let x', y', z' be the coordinates of an interior point in the basin, where

$$\left.\begin{matrix} 0 < x' < 3a/2, \\ y_1' < y' < y_2', \\ -H < z' < 0; \end{matrix}\right\} \qquad (2.11)$$

a is the radius of the earth. Both the normal and parallel velocity components vanish at the wall, which is also taken to be a perfect insulator.

$$u' = v' = \vartheta_x' = 0 \quad \text{for} \quad x' = 0, 3a/2, \qquad (2.12)$$

$$u' = v' = \vartheta_y' = 0 \quad \text{for} \quad y' = y_1', y_2'. \qquad (2.13)$$

As a simplification of the model, bottom friction is neglected and free slip is allowed at the lower boundary.

$$w' = u_z' = v_z' = \vartheta_z' = 0 \quad \text{for} \quad z' = -H. \qquad (2.14)$$

At the upper boundary,

$$\left.\begin{matrix} w' = v_z' = 0 \\ \vartheta' = \vartheta^*(y) \\ \varkappa u_z' = \tau^*(y) \end{matrix}\right\} \quad \text{for} \quad z' = 0. \qquad (2.16)$$

The condition that w is equal to zero at the surface is frequently called the "rigid lid" approximation. It has the advantage of filtering out external gravitational-inertial oscillations. The asterisks denote distributions of temperature and stress specified at the upper boundary. The variation of ϑ^* and τ^* with respect to latitude is shown in Fig. 2b.

In scaling the equations we will make use of ideas developed in previous studies of ocean circulation (ROBINSON, 1960). It is anticipated that the abyssal temperature below the thermocline will coincide with the minimum temperature specified at the surface adjacent to the north wall. Let d be defined as the scale depth of the thermal boundary layer. If $\Delta\vartheta^*/a$ is the north-south temperature gradient specified at the surface, a measure of the vertical temperature gradient is given by $\Delta\vartheta^*/d$. In addition two scale velocities may be defined in terms of external parameters.

V^* will represent the component depending on the density gradient at the surface, while the component due to wind stress will be designated as V^{**}. In order to define V^*, the geostrophic relation is differentiated with respect to the vertical coordinate. Substituting the hydrostatic relation,

$$2\Omega V^*/d = g\alpha\Delta\vartheta^*/a. \tag{2.17}$$

SVERDRUP (1947) was able to show from actual observations that a linearized, and vertically integrated version of the vorticity equation could be used to calculate the meridional mass transport in open ocean areas. For purposes of defining a scale velocity it will be assumed that the mass transport takes place within the thermal boundary layer. For this case Sverdrup's formula,

$$\beta \int_{-H}^{0} \varrho v dz = \text{curl } \bar{\tau},$$

where β is the latitudinal variation of the coriolis force, may be written as

$$\varrho_0 \frac{2\Omega}{a} V^{**} d = \omega^*. \tag{2.18}$$

$2\Omega/a$ is a measure of β, while ω^* is the maximum latitudinal gradient of the surface wind stress distribution shown in Fig. 2.

The thermal boundary layer may be defined as a region in which thermal diffusion normal to the surface and advection are of the same order. In terms of scale parameters,

$$V^*\Delta\vartheta^*/a = \varkappa\Delta\vartheta^*/d^2. \tag{2.19}$$

As shown by the work of STOMMEL & WEBSTER (1962) the wind may either cause a decrease or an increase in depth of the thermocline, depending on whether the wind pattern is such as to cause a local upwelling or downwelling, respectively. For this reason the wind component has not been included in the definition of the scale depth, d, which may be obtained by combining (2.17) and (2.19).

$$d = \left(\frac{2\Omega\varkappa a^2}{g\alpha\Delta\vartheta^*}\right)^{\frac{1}{3}}. \tag{2.20}$$

It should be noted that the simplifications introduced in (2.17)–(2.20) do not involve restrictive assumptions on the model itself. They are only used to define V^*, V^{**}, and d in terms of external parameters in a manner suited to the time-averaged flow observed in the ocean.

Substituting the dimensionless variables

$$u', v', w' = V^*u,\ V^*v,\ V^*dw/a,$$

$$x', y', z' = ax,\ ay,\ dz,$$

$$t' = ta/V^*,$$

$$\vartheta' = \Delta\vartheta^*\vartheta,$$

$$p'/\varrho_0 = 2\Omega a V^* p$$

in (2.1)–(2.5), we obtain

$$\text{Ro}\,(Du - mnuv - u_{zz}) = nv - mp_x + m^2 \frac{\text{Ro}}{\text{Re}} \nabla^2 u, \tag{2.21}$$

$$\text{Ro}(Dv + mnuu - v_{zz}) = -nu - mp_y + m^2 \frac{\text{Ro}}{\text{Re}} \nabla^2 v, \tag{2.22}$$

$$\vartheta = p_z + \text{const }(z), \tag{2.23}$$

$$D\vartheta = \frac{1}{\delta}\vartheta_{zz} + \frac{m^2}{\text{Pé}} \nabla^2 \vartheta, \tag{2.24}$$

$$w_z = -m^2[(u/m)_x + (v/m)_y]. \tag{2.25}$$

The non-dimensional constants Ro, γ, Re and Pé are defined as follows:

$\text{Ro} = V^*/(2\Omega a)$	= Rossby number	(2.26)
$\gamma = (V^* + V^{**})/V^*$	= wind parameter	(2.27)
$\text{Re} = V^*a/A_M$	= effective external Reynolds number	(2.28)
$\text{Pé} = V^*a/A_H$	= effective external Péclèt number	(2.29)

The term "effective" is used here because it is the Reynolds number associated with lateral turbulent mixing. "External" is used to indicate that the Reynolds number is based on the scale velocity outside, rather than inside, boundary current regions.

A fifth important parameter comes in through the bottom boundary condition. This is H/d, the ratio of the total depth to the scale depth of the thermocline.

For the numerical methods the author is very much indebted to investigations by ARAKAWA (1963) and LILLY (1965). Details are given in Appendix B.

3. Oceanographic interpretation of the non-dimensional parameters

The reduction of the equations to non-dimensional form greatly reduces the number of numerical calculations required to investigate the system. To insure that this formulation of the problem does not obscure the geophysical interpretation of the results, several tables have been prepared to relate the non-dimensional parameters to more familiar physical quantities. In Table 3.1 d is given as a function of $\varkappa$ and $\Delta\vartheta^*$. The following quantities are taken to be fixed,

$$\alpha = 2.5 \times 10^{-4}/\text{deg.}, \quad g = 10^3 \text{ cm/s}^2,$$

$$a = 6.37 \times 10^8 \text{ cm}, \quad 2\Omega = 1.458 \times 10^{-4}/\text{s}.$$

Note that because of the cube root dependence, large variations of $\varkappa$ have a relatively small effect on d and the ratio, H/d. In Table 3.2 the Rossby number, Ro, is given for exactly the same parameters. An approximate value of the corresponding scale velocity, V^*, in cm/s can be obtained by multiplying Ro by 10^5.

The correspondence between the Reynolds number and various values of the lateral mixing coefficient is given in Table 3.3. The coefficient of vertical diffusion has a fixed value of 5 cm²/s. The same table may also be used to determine the Péclèt number by simply replacing A_M by A_H.

In a final table the wind parameter, γ, is given as a function of the maximum transport in the western boundary current needed to balance the Sverdrup transport southward in the interior. As in the previous table it is assumed that $\varkappa$ has a fixed value of 5 cm²/s.

TABLE 3.1. *The scale depth, d, given in meters, for different values of $\varkappa$ and $\Delta\vartheta^*$ computed from equation (2.20).*

$\Delta\vartheta^*$	$\varkappa =$ 0.2 cm²/s	1 cm²/s	5 cm²/s
9°	174	297	508
18°	138	236	403
27°	120	206	352

TABLE 3.2. *The Rossby number for different values of $\varkappa$ and $\Delta\vartheta^*$ computed from equation (2.26).*

$\Delta\vartheta^*$	$\varkappa =$ 0.2 cm²/s	1 cm²/s	5 cm²/s
9°	0.46×10^{-5}	0.78×10^{-5}	1.33×10^{-5}
18°	0.72×10^{-5}	1.24×10^{-5}	2.12×10^{-5}
27°	0.95×10^{-5}	1.62×10^{-5}	2.78×10^{-5}

TABLE 3.3. *The effective Reynolds number for different values of A_M.*

$\Delta\vartheta^*$	$A_M =$ 10⁷ cm²/s	10⁸ cm²/s	10⁹ cm²/s
9°	78	8	1
18°	125	12	1
27°	164	16	2

TABLE 3.4. *The wind parameter, γ, as a function of $\Delta\vartheta^*$ and the integrated mass transport in the western boundary current computed from Sverdrup's formula.*

	Mass Transport (10⁶ tons/s)		
$\Delta\vartheta^*$	0	38	113
9°	1.0	2.1	4.4
18°	1.0	1.7	3.2
27°	1.0	1.5	2.6

4. Discussion of the results

In comparing the results of calculations for different cases it is useful to have a non-dimensional expression for the poleward heat transport in the model ocean basin. One form may be obtained by dividing the total heat transport by the amount of heat that would be transferred by lateral mixing alone down the gradient of temperature which is specified through the

TABLE 4.1. *HT^* given by equation (4.2) for different values of $\varkappa$ and $\Delta\vartheta$. The remaining constants have the fixed values given in section 3. Units are 10^{14} cal/s.*

$\Delta\vartheta^*$	$\varkappa =$ 0.2 cm²/s	1 cm²/s	5 cm²/s	25 cm²/s
9°	0.42	1.23	3.59	10.51
18°	1.06	3.09	9.06	26.50
27°	1.82	5.32	15.55	45.50

surface boundary condition. Let HT be the total poleward heat flux at a given latitude.

$$\eta = HT/(A_H a d \Delta\vartheta^*/a). \tag{4.1}$$

Another form may be obtained which is independent of the parameter, A_H, by simply dividing η by Pé.

$$HT/HT^* \equiv HT/(\varkappa a^2 \Delta\vartheta^*/d). \tag{4.2}$$

HT^* is given for various values of $\varkappa$ and $\Delta\vartheta^*$ in Table 4.1. In general η and HT/HT^* are functions of latitude and time as well as the five dimensionless parameters of the model given in the preceding section.

Initial conditions for the calculations were chosen to be a state of horizontally uniform stratification and complete rest. The initial temperature field of the calculations is given in Table 4.2. At the beginning of the calculation, deep convection occurs near the north wall due to the relatively low temperatures specified at the surface. This sets up lateral density gradients within the fluid. East-west currents arise almost instantaneously, followed by adjustments leading to the formation of a northward-moving surface current at the western boundary.

In Fig. 3 the heat transport at a latitude of 45° is plotted as a function of time. For the dimensionless parameters given in Table 4.3 an approach to an equilibrium steady state is indicated in all cases.

TABLE 4.2. *The initial, horizontally uniform temperature field.*

z	0.3	0.6	1.3	2.6	5.2	10.4
ϑ	0.67	0.55	0.44	0.28	0.03	0.00

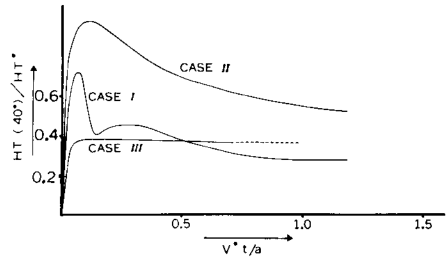

FIG. 3. The behavior of the total poleward transport of apparent heat at a latitude of 45°. Curves for cases II, III and I correspond to strong, moderate and weak mixing of apparent temperature.

Even in the range considered (Re $\leqslant$ 8, Pé $\leqslant$ 32) it is obviously impossible to completely explore the behavior of the circulation as a function of all five independent parameters. Instead, the eight different cases of Table 4.3 are chosen to examine the first order variation due to each one of these parameters with a purely thermal circulation chosen as a reference state.

The refined net referred to in Table 4.3 is described later in connection with the results of Cases IV and V.

a. Variation of the thermal diffusion coefficient, Pé.

The parameters for the reference state are given under Case I in Table 4.3. The equilibrium solutions for different cases will be considered in groups. Except for the particular parameter under consideration, the nondimensional numbers will in general have values identical to Case I. The effect of the Péclèt number, a measure of the lateral mixing of heat, is illu-

TABLE 4.3. *Dimensionless parameters of the calculations. In the last column, U indicates the uniform 17 × 17 net, R indicates a net with extra resolution at the western wall.*

Case	Pé	γ	Re	H/d	Ro	Net
I	32	1.0	8	13	3×10^{-5}	U, R
II	2	1.0	8	13	3×10^{-5}	U
III	8	1.0	8	13	3×10^{-5}	U
IV	32	1.9	8	13	3×10^{-5}	R
V	32	3.9	8	13	3×10^{-5}	R
VI	32	1.0	0.8	13	3×10^{-5}	U
VII	8	1.0	8	130	3×10^{-5}	U
VIII	32	1.0	8	13	3×10^{-3}	U

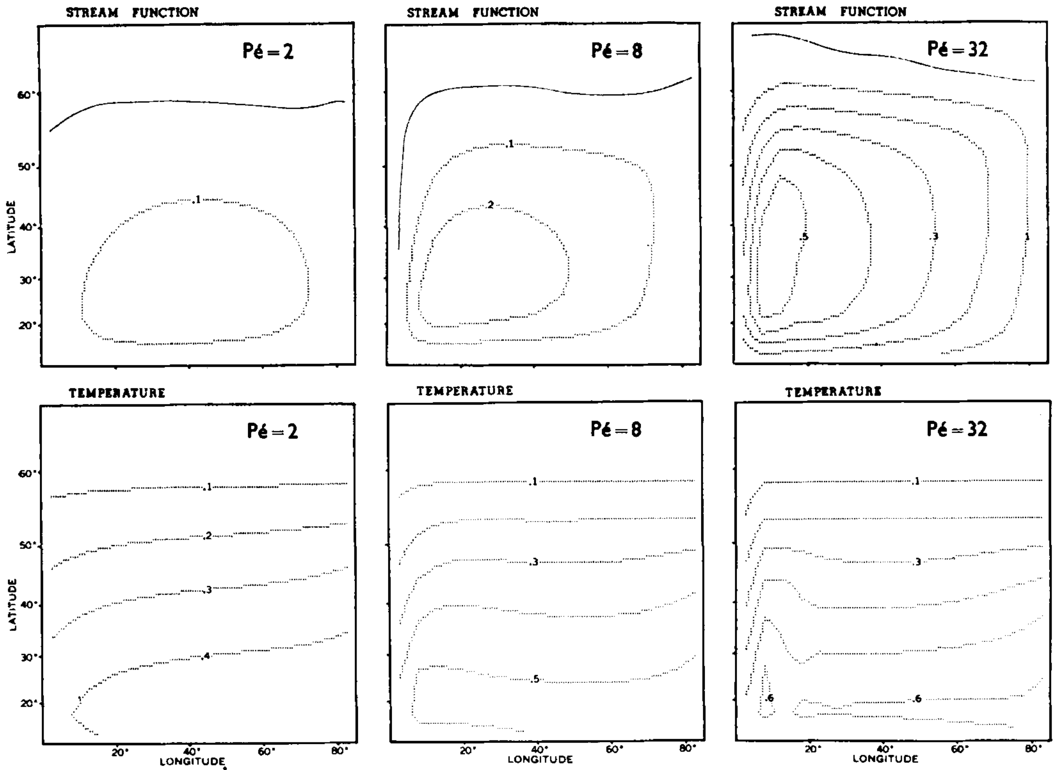

FIG. 4. Horizontal patterns of stream lines and temperature at $z = -0.6\ d$ corresponding (from left to right) to cases II, III and I. Pé = 2, 8 and 32 indicate strong, moderate and weak lateral mixing of apparent temperature. Other parameters are held constant.

strated in Cases I, II and III. These three cases cover a range from 2 to 32, or a total variation of Pé by a factor of 16.

We see from Fig. 3 that convergence in Case II is not complete, but note that the difference in heat transport corresponding to a change in Pé from 2 to 8 is as great or greater than the difference in heat transport corresponding to a change in Pé from 8 to 32. The fact that a change of 6 in the low range is equivalent to a change of 24 in a higher range of Pé may be explained by the diminishing importance of lateral mixing in the total heat transport. Except for the region just adjacent to the northern wall, lateral mixing accounts for less than 10 % of the poleward heat transport for Pé equal to 32.

The horizontal patterns of stream lines and temperature at a level 0.6 *d* below the surface is shown for these cases in Fig. 4. The patterns are taken from the solution corresponding to the end points of the curves in Fig. 3. The streamlines and isotherms in Fig. 4 and subsequent figures are taken directly from the typewritten machine output based on linear interpolation without any further modification. For Pé equal to 2 the streamline pattern for the nondivergent component of the flow at this level is very weak and nearly symmetric with respect to a meridian down the center of the basin. As Pé increases, the circulation strengthens and western intensification becomes more evident. The main features of the pattern for Pé equal to 32 (Case I) correspond to the theoretical outline of a thermohaline circulation given by STOMMEL (1958) in *The Gulf Stream*. The boundary current is different from that of the wind-driven ocean theories. No appreciable vertically integrated mass transport takes place along the western boundary. The northward flow in the upper layers is compensated by a narrow and deep, southward moving boundary current at the bottom. More detail is given in the next subsection in connection with Fig. 12.

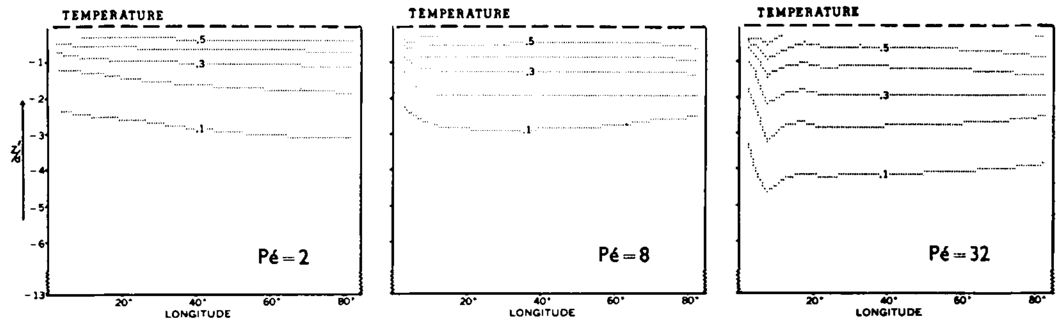

FIG. 5. East-west sections of apparent temperature shown for a latitude of 32° N, corresponding to the patterns in Fig. 4.

The temperature patterns in Fig. 5 indicate that the thermal layer deepens as Pé grows larger. The movement of the temperature maximum at this level out from the south wall with increasing Pé accompanies the strengthening of an anticyclonic gyre. Another feature of interest is the suggestion of a warm core adjacent to the western boundary current.

Although the streamlines indicate southward flow over most of the interior, in the northern part of the basin this flow is more than compensated by a divergent component moving into a region of strong downward motion in the northeast corner of the basin. Warm advection by this upper branch of the meridional circulation brings water into areas in which a lower temperature is specified at the surface. The rigid east-west trend of the isotherms indicates that they are closely tied to the temperature specified at the surface by the free convective mechanism of the model in (2.10).

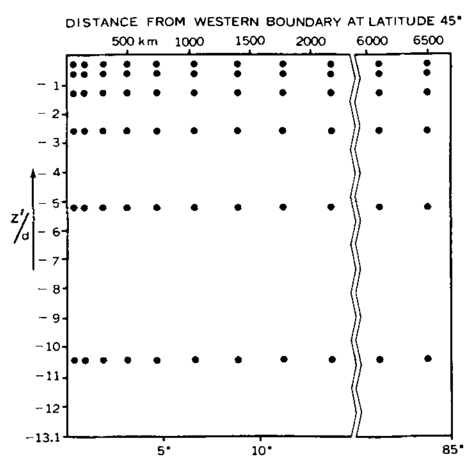

FIG. 6. The pattern of grid points is shown in a vertical, east-west plane for the refined net.

Further insight into the dependence of the three-dimensional temperature patterns on the parameter Pé is given by the vertical temperature section at a latitude of 32° given in Fig. 5. The buildup of the western boundary current as Pé increases is very clearly indicated. While the isotherms have a nearly uniform slope downwards towards the eastern wall for Pé equal to 2, the isotherms are concave upward at the lower levels for Pé equal to 32 (Case I). This pattern is associated with an anticyclonic gyre which is almost entirely suppressed by mixing in Cases II and III.

b. *Variation of the wind stress parameter*, γ

The most interesting results of the entire study may be obtained through a detailed comparison of Cases I, IV and V. Case IV and V indicate the effect of a zonally uniform wind stress in modifying the purely thermal circulation of the reference case. In cases which include a wind-driven component of the circulation it becomes clear that the regular 17×17 net used in the other calculations is no longer adequate to resolve the boundary current in a realistic range of the parameters. For this reason the resolution is increased in the x-direction in the immediate vicinity of the western wall while the numerical net in the interior is unmodified. The irregular net is formulated in such a way that the advective transport terms conserve linear and quadratic quantities in the same manner as the regular net. The simple principle involved is given in a separate reference (BRYAN, 1965). The spacing of grid points in the x- and z-directions is shown in Fig. 6.

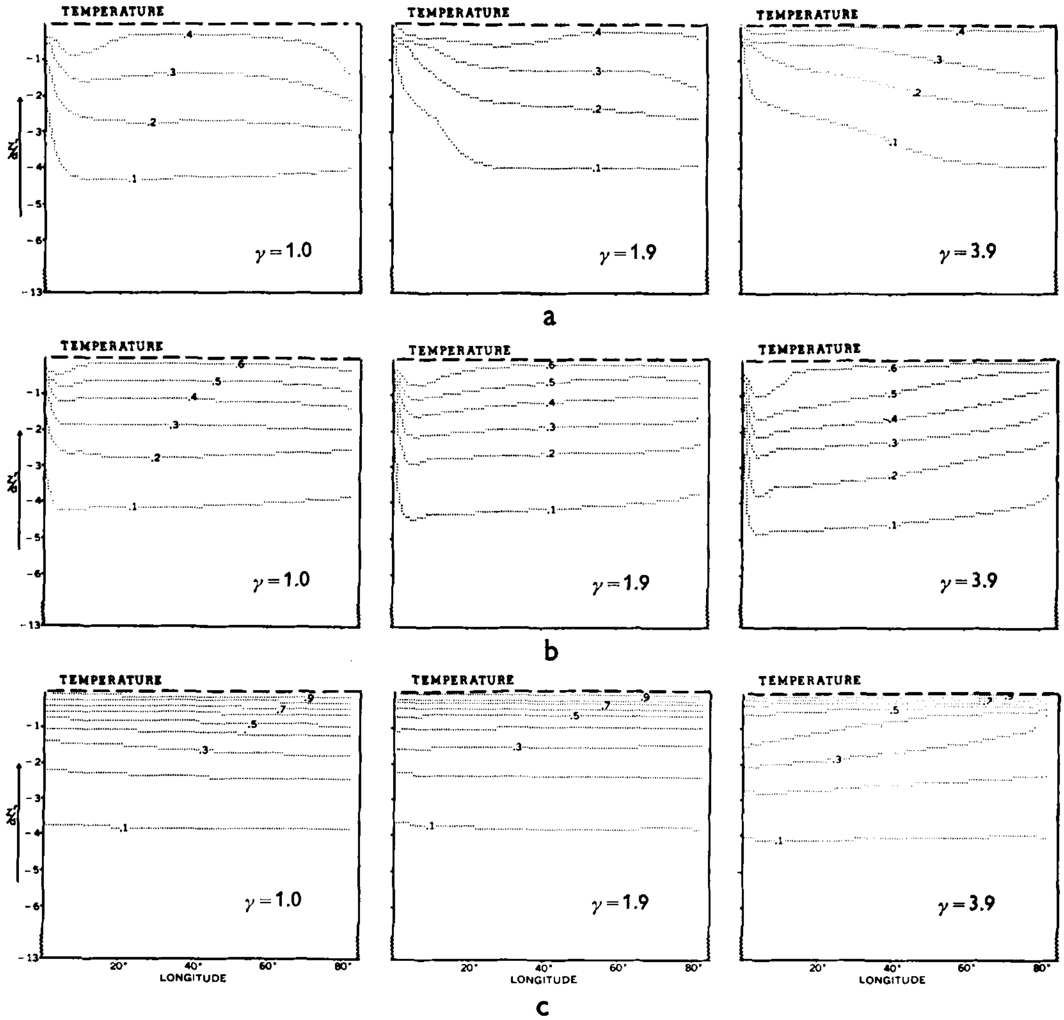

FIG. 7. East-west temperature sections for the final solutions. From left to right the patterns correspond to Cases I ($\gamma = 1.0$, no wind), Case IV ($\gamma = 1.9$, intermediate wind), Case V ($\gamma = 3.9$, strong wind). The latitudes of the sections are (*a*) 44°, (*b*) 32° and (*c*) 12°.

In order to make the reference case strictly comparable, Case I has been recomputed using the refined net at the western boundary. Some idea of the effect of this additional resolution may be obtained by comparing the east-west temperature section designated by $\gamma = 1$ in Fig. 7*a* to the reference section in Fig. 5 (extreme right). Note that in Fig. 5 an exaggerated warm core appears at lower levels which is not present for the same case computed with higher resolution.[1]

[1] A reviewer has correctly pointed out that the addition of extra resolution on the western boundary may introduce a bias in the solutions. This bias would favor a western boundary current over a possible eastern boundary current. This point can only be settled conclusively by much more detailed calculations using a finer net. However, it can be seen that a pronounced western boundary current already appears in calculations with a uniform grid (see Fig. 5). The calculations are restricted to viscous regimes (Re ≤ 8) in which small scale features are strongly damped. If the continuous solutions in this viscous range contained a strong eastern boundary current, some indication should appear in the numerical calculations with the grid used in the present study, particularly in Case VIII (Fig. 15) in which the resolution is more than adequate to resolve the boundary regions.

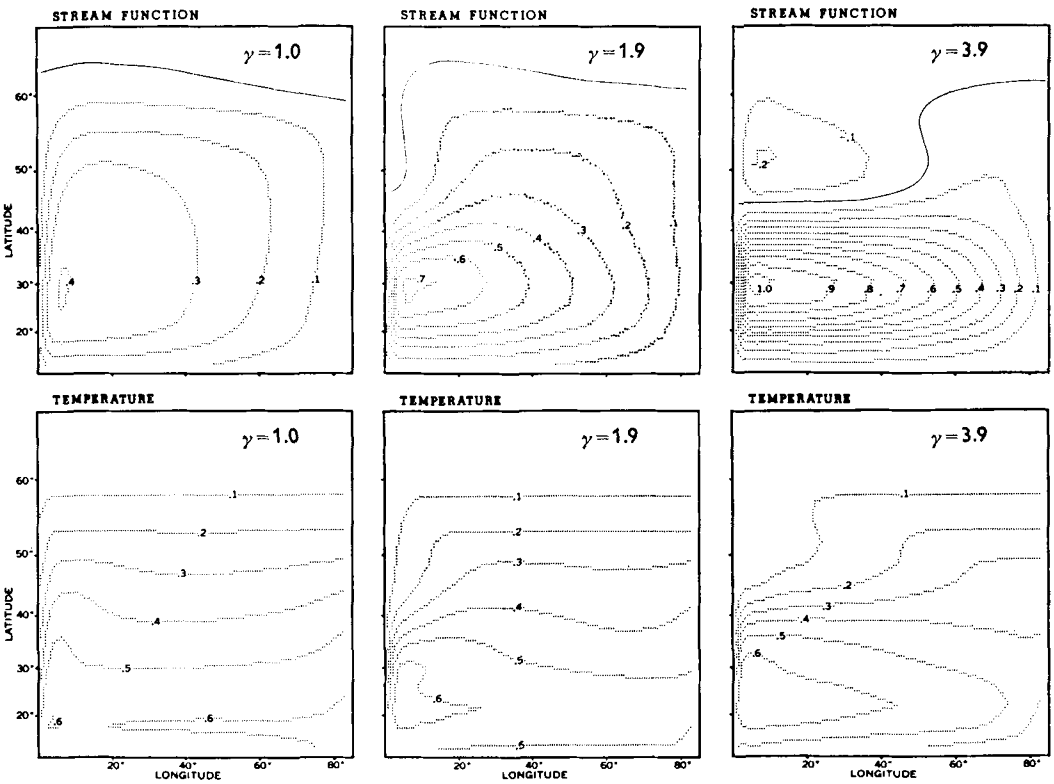

FIG. 8. Horizontal patterns of the stream lines and temperature at $z = -0.6\ d$ corresponding to Fig. 7.

In Fig. 1 east-west vertical density sections are shown for the North Atlantic based on IGY data. For comparison similar apparent temperature sections are shown corresponding to Cases I, IV and V in Fig. 7a. Sections are shown for a latitude of 44° in Fig. 7. They indicate that the addition of wind brings the patterns into much better agreement with observations. In case I the warm core at the western boundary indicates the extension of the western boundary current into subarctic latitudes. The wind stress pattern shown in Fig. 2, however, forces the western boundary current away from the coast at this latitude. The patterns for $\gamma > 1$ in Fig. 7*a* show a gentle east-west slope of the isotherms which is associated with a broad northward drift of surface water extending across the entire section.

Cross-sections for a latitude of 32° are shown in Fig. 7*b*. These sections cut directly through the subtropical gyre. Note that in the purely thermal circulation of the reference case the isotherms are relatively horizontal across the interior except at the base of the thermocline. When wind is introduced, the gyre intensifies and a warm water lens forms on the western side of the basin, which gives the isotherms the characteristic slope upward to the east near the surface indicated in the IGY section of Fig. 1*b*. The thermocline solution of ROBINSON & STOMMEL (1959), on the other hand, implies that the observed east-west slope of the σ_t surfaces may be produced by a purely thermal circulation. The apparent discrepancy between the Robinson and Stommel study and the present calculations may be traced principally to differences in lateral boundary conditions. This point is discussed briefly in Appendix A.

The temperature sections at the south wall of the basin shown in Fig. 7*c* may be compared in a general way to the IGY section at 8° N in Fig. 1. Detailed comparison is not appropriate because there is a strong flow of surface water into the North Atlantic which is not included in our model. Note in Fig. 7c that the wedge of warm water thinning to the east is only present for $\gamma > 1$.

A comparison of the horizontal pattern of temperature and the nondivergent component of velocity for cases with and without wind may be made from Fig. 8. This figure is made for a level 0.6 d below the surface. From Table 3.1 it may be seen that this level would correspond to approximately the 200 meter level in the real ocean. The streamline patterns show how the single large anticyclonic gyre of Case I splits into a subtropical and subarctic gyre where the wind effect has its maximum value. The thermal and wind effects work in the same direction in the subtropical gyre, but tend to oppose each other in the subarctic gyre region. For this reason the subarctic gyre is relatively weak. In the case in which the wind effect is strongest it may be noted that the subtropical gyre is nearly symmetric with respect to an east-west axis along latitude 30°. Models of a homogeneous ocean indicate that nonlinear terms in the momentum equations destroy a north-south symmetry in the stream lines. Thus the patterns in Fig. 8 probably indicate that the Reynolds number is too low to allow the nonlinear terms to be significant in the momentum equations. On the other hand, it is evident from the character of the horizontal temperature patterns that the relatively high value of the Péclèt number does allow advective terms to be important in the thermal equation.

As a basis for comparison the observed temperature pattern for the North Atlantic at 200 meters based on the *Meteor Atlas* is shown in Fig. 9. One of the most striking features of

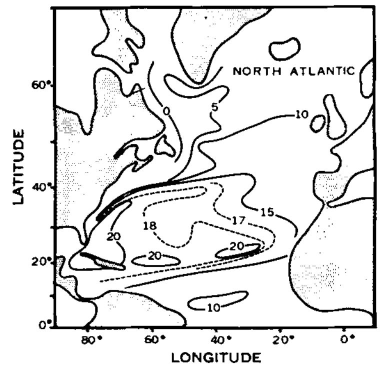

FIG. 9. The observed temperature pattern at a level 200 m below the surface in the North Atlantic based on *The Meteor Atlas* (WÜST & DEFANT, 1936).

the observed pattern is the concentration of isotherms at mid-latitudes near the western boundary and the relatively weak temperature gradient at the same latitude along the eastern boundary. This general tendency is captured in the temperature pattern of Fig. 8 corresponding to γ equal to 3.9. Another feature of interest in this computed pattern is the small region of low temperature in the southeast corner of the basin. This region of low temperature apparently corresponds to the observed tendency for upwelling to occur along the eastern edges of the North Atlantic and Pacific in the trade wind belt.

A close relationship is indicated between many features of the temperature pattern shown in Fig. 8 and the vertical velocity fields of Fig. 10. Due to a difference in order of magnitude in the vertical velocity near the boundaries relative to the interior, the vertical velocity is contoured using a logarithmic scale. In the

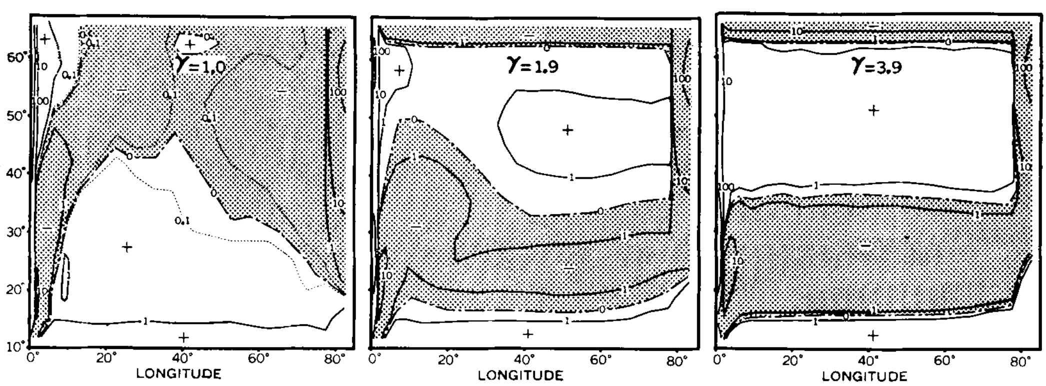

FIG. 10. Vertical velocity at $z = -0.6\ d$, corresponding to the patterns in Fig. 8.

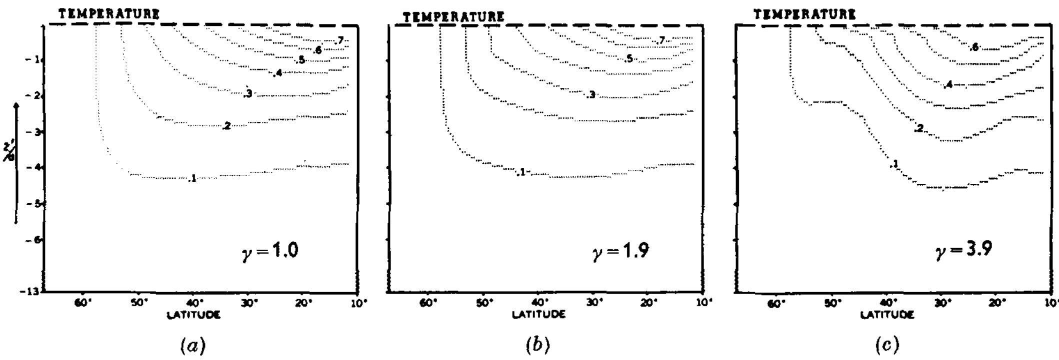

FIG. 11. North-south sections bisecting the basin. $\gamma = 1$, 1.9 and 3.9 correspond to negligible, moderate and strong wind stress over the model ocean.

case of a pure thermal circulation without rotation, it might be expected that flow would be directed down the pressure gradient. With the boundary condition on temperature used in these computations the result would be zonally symmetric overturning with rising motion at low latitudes and northward movement at the surface. The effect of rotation is to induce flow along lines of constant pressure rather than across them. The temperature gradient imposed at the surface forces a strong eastward geostrophic flow. Continuity requires a strong upward motion at the west wall and a strong downward motion at the east wall to balance this flow. Thus the effect is to modify the thermal circulation by rotating it clockwise so that the center of rising motion is in the southwest corner of the basin and the center of sinking motion is in the northeast corner.

Strong vertical velocities occur only along the lateral walls when no wind is present due to the strong constraint of rotation which supresses divergent flow. Wind stress introduces a nongeostrophic component in the interior, producing strong upwelling and downwelling in the subarctic and subtropical wind gyres, respectively. As might be expected, the effect of wind on the vertical velocity fields diminishes with depth. At the base of the thermocline the vertical velocity patterns (not shown) are very much the same for different values of γ. Note that the region of maximum sinking in the northeast corner in Fig. 10 is very much the same for all three cases. Observational studies indicate that the region of maximum sinking lies along Greenland on the western side of the North Atlantic, rather than on the east side as indicated by the calculations. Calculations taking into account the exact shape of the North Atlantic basin, and a wind stress pattern based on actual wind observations are needed to resolve this point.

Vertical temperature sections made in a meridional plane dividing the east and west half-basins are shown in Fig. 11. Even in the case of a purely thermal circulation there is a tendency for the isotherms to be bowed downward. This is in agreement with the results of ROBINSON & STOMMEL (1959). The effect of wind is to greatly accentuate this tendency. The thermocline becomes shallower in both low and high latitudes. A quantitative comparison with the observed thermocline depth of the North Atlantic is made in the following section.

A more complete idea of the changes in circulation caused by wind is given in Fig. 12*a*, *b* and *c*. The *u*- and *v*-components of velocity are given in vertical cross sections which extend to the bottom, allowing an examination of the abyssal circulation. The sections in an east-west plane are located at 32°, cutting right through the center of the subtropical gyre. In the reference case ($\gamma = 1$) the zero line in the interior separating southward drift at the surface from northward drift below occurs at mid-depths. Reversal of flow takes place at a somewhat higher level in the vicinity of the western wall. For a reasonable choice of oceanographic parameters (see Table 3.2) the scale velocity would be about 2 cm/s. The core of western boundary current would then be about one hundred kilometers wide and moving at a velocity of 20 cm/s. As wind is introduced the core velocity is increased to 3 times this value, but the velocity of the deep countercurrent flowing to the south along the bottom re-

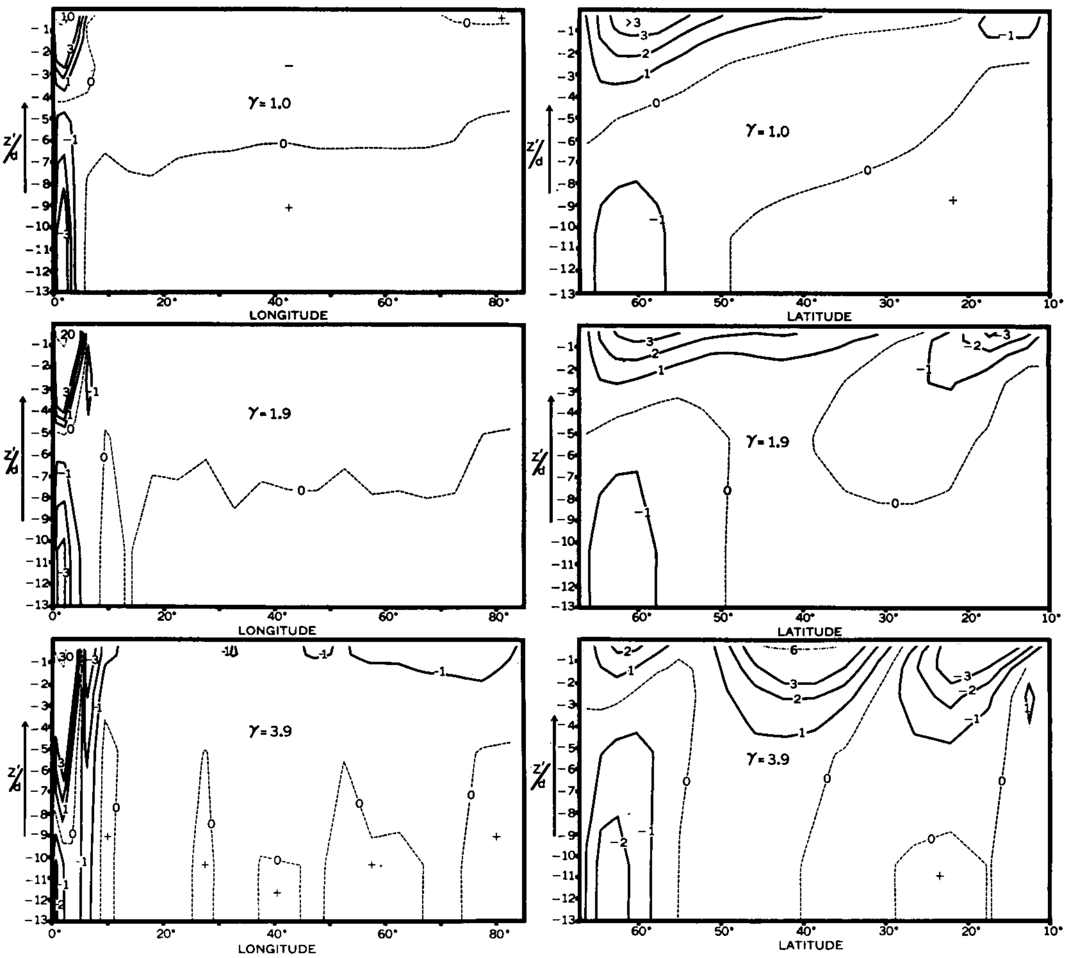

FIG. 12. The effect of the wind stress pattern on the velocity field is shown. (*Left*) East-west sections of the meridional component of velocity in nondimensional units. (*Right*) North-south sections of the zonal velocity components. The east-west sections are at a latitude of 32° and the north-south sections at a longitude of 42.5°. *a*, Case I (no wind, $\gamma = 1$); *b*, Case IV (moderate wind, $\gamma = 1.9$); *c*, Case V (strong wind, $\gamma = 3.9$).

mains about the same as that of the reference case.

Another effect of wind is to push the region of southward drift in the interior downward until it penetrates to the bottom at some points. Geostrophic considerations require that the southward velocity component increase upward in cases where the isotherms tilt upward toward the eastern wall. The temperature patterns of Fig. 7*b* show that for γ equal to 1 the tilt of the isotherms is confined to the base of the thermocline. Within the thermocline itself the isotherms are nearly horizontal. As a result the southward flow shown in Fig. 12 is nearly uniform with respect to depth above the base of the thermocline for γ equal to 1. With wind the isotherms within the subtropical gyre strongly tilt up to the east, as noted previously. This tilt is associated with an increase of southerly flow right up to the surface. A maximum southerly flow occurs right at the east wall near the surface where a shallow region of weak northerly flow exists in the purely thermal solution.

The north-south sections in Fig. 12 are in exactly the same plane as the temperature sections in Fig. 11. It may be seen that in the reference case the anticyclonic circulation is

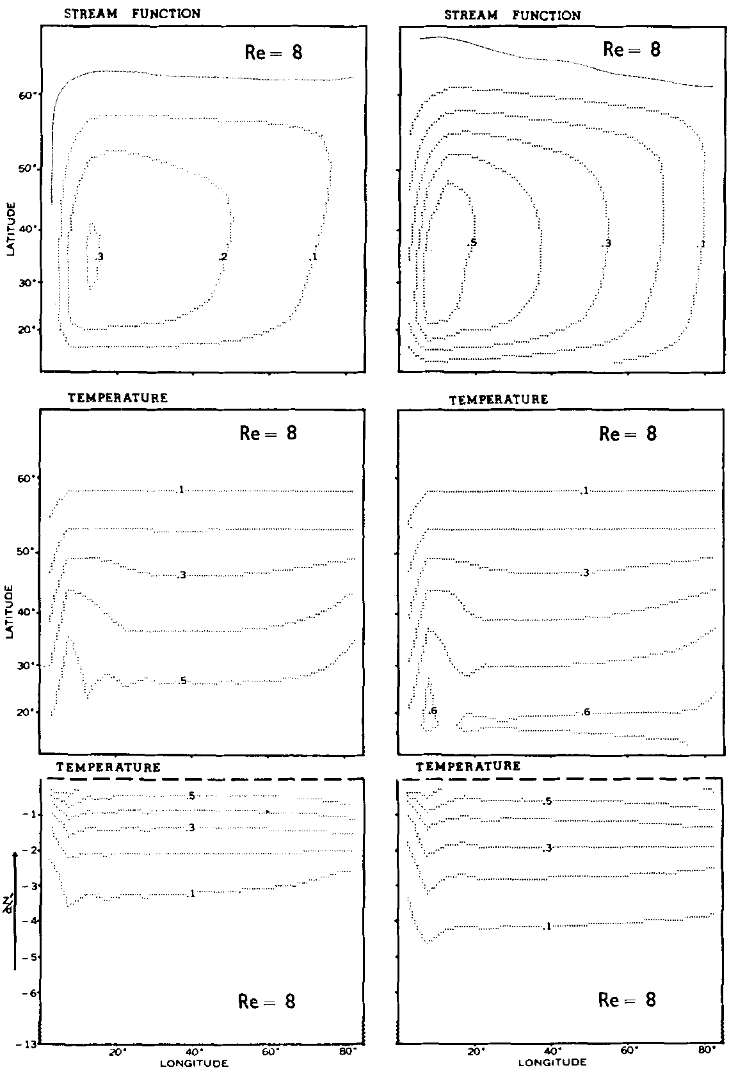

FIG. 13. The effect of a variation in Reynolds number in the horizontal patterns of stream lines and temperature at $z = -0.6\ d$. (*Below*) East-west vertical temperature sections at 32° of latitude. Re = 0.8 and 8 correspond to strong and intermediate horizontal mixing of momentum, respectively.

very shallow. At the surface, drift to the east extends over most of the section with return flow to the west confined to a narrow region adjacent to the south wall. The effect of wind is seen to be a deepening of the anticyclonic gyre in subtropical latitudes. In middle latitudes drift to the east, forming an extension of the western boundary current, penetrates all the way to the bottom for $\gamma > 1$. Other sections (not shown) indicate that the deep countercurrent below the western boundary current remains close to the boundary north of the point at which the surface current leaves the wall, moves seaward and deepens.

c. *Variation of the momentum diffusion parameter, Re*

The calculations of the present study are restricted to the most accessible, low range of Reynolds number. Some effects which take place within the range of the Reynolds number from 0.8 to 8 are shown in Fig. 13. As in the other figures the horizontal patterns are taken at a depth 0.6 *d* below the surface. Note that the intensity nearly doubles and the western boundary current becomes much narrower for Re equal to 8. The temperature patterns in the horizontal plane are very similar, however. The principal modification of the temperature field that takes place is shown in the vertical sections made in the zonal plane at a latitude of 32°. The thermocline is pushed downward in the case of the more vigorous circulation associated with the higher Reynolds number case. Based on experience with similar computations for a homogeneous, wind-driven ocean model (BRYAN, 1963) nonlinear effects in the momentum equations do not become significant until the Reynolds number is in the range of 50–100.

d. *Variation of the depth parameter, H/d*

Some idea of the effect of a variation in H/d may be obtained on the basis of Cases III and VII. In these two cases H/d has the value of 13 and 130 respectively. They differ from Case I in that the Pé is 8 instead of 32. The results indicate surprisingly little difference in the two solutions in the upper layers. In Figure 14 the difference in heat transport is plotted as a percentage of the maximum value. The maximum percentage difference does not amount to more than a few per cent at any latitude. The temperature patterns (not shown) are also very similar. A conclusion to be drawn from this is that H/d equal to 13 is near the asymptotic range. Further increases in H/d, no matter how large, do not lead to significant changes in the circulation. This corresponds to a conclusion reached by STOMMEL & WEBSTER (1962) based on thermocline calculations. It should be noted that this result is probably not valid for cases with wind or bottom friction. In such cases a net vertically integrated mass transport is present. The strength of the currents will depend critically on whether the total mass transport is distributed through a shallow or very deep column of water.

e. *Variation of the rotational parameter, Ro*

In Case VIII a calculation is carried out for Ro two orders of magnitude larger than the reference case. If other constants were kept the same this would correspond to a rotation

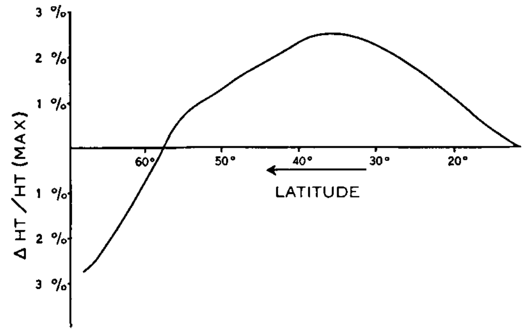

FIG. 14. The difference between the poleward heat transport of Case VII (H/d = 130, nearly infinite total depth) and Case III (H/d = 13, moderate total depth). The ordinate is the percentage of the heat transport at 45°.

of the earth only once every 100 days. Although this case is completely out of the geophysical range, the large variation of Ro helps to isolate the dependence of the solutions on this parameter. Patterns of the stream function, temperature and vertical velocity for Case VIII are given in Fig. 15, corresponding to a level 0.6 *d* below the surface.

The formation of a western boundary current depends on the latitudinal variation of the coriolis parameter (the "beta" effect). Since the Rossby number is inversely proportional to rotation, a larger Rossby number implies a weaker beta effect. Linear theory for a wind-driven ocean model with lateral eddy viscosity indicates that the width of the boundary current is inversely proportional to the cube root of the beta parameter (STOMMEL, 1958, p. 97). The cube root of 100 is 4.6. A detailed examination of the solutions indicates that in agreement with the simplified theory the western boundary current at a latitude of 32° is 4–5 times wider for Case VIII than in Case I computed with the refined grid.

In other features the stream line and temperature patterns of Case VIII and the reference case are quite similar. Since the boundary current is much broader, it is also less intense. Consequently the effect of lateral advection is much less evident near the western boundary. Only a suggestion of a warm core appears in the temperature pattern of Fig. 15.

In the other cases a region of intense vertical motion takes place adjacent to the lateral walls. It is impossible to adequately resolve these vertical velocity fields. In Case VIII, however,

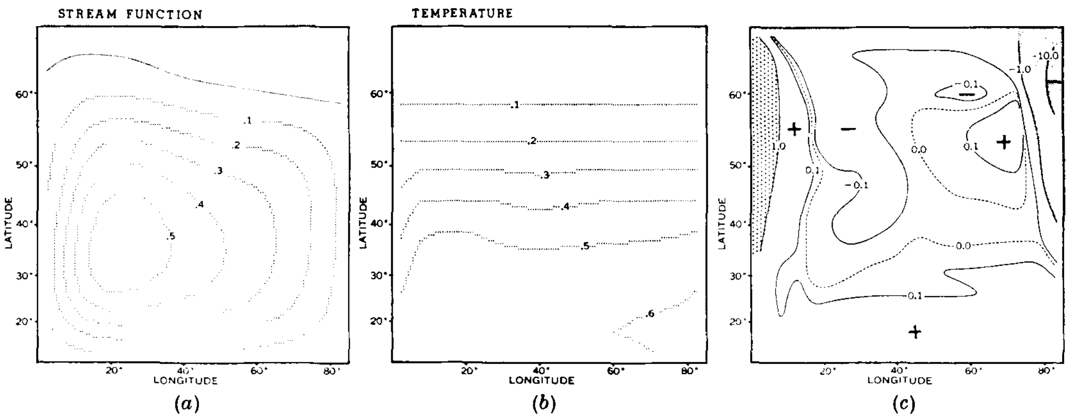

FIG. 15. Horizontal patterns of (a) stream function, (b) temperature and (c) vertical velocity are given for Case VIII (large Rossby number).

these regions of intense vertical motion are wide enough to be fairly well resolved by the regular 17×17 net. It is reassuring to note that at least in the vicinity of the walls the general pattern of vertical velocity remains much the same. The maximum vertical velocities are much less, but that is to be expected since the areas involved are so much wider.

Case VIII appears to indicate that the rotational constraint is so large that the steady state circulation is a nearly asymptotic regime with respect to Rossby number. Substantial variations of Ro about its actual value will alter the width of the boundary current, but will not change the essential character of the thermal circulation.

5. Comparison with North Atlantic data

Due to obvious differences between model and prototype there are difficulties in relating various features of the solutions to corresponding features of the North Atlantic. Such a comparison, however, offers the best quantitative test of the results. Three quantities will be considered. The first to be discussed is a measure of the depth of the thermal boundary layer at the surface. This measure will be designated as ξ, and it will be defined as the depth at which the temperature drops to $\frac{1}{2}$ its surface value at a latitude of 20° in the middle of the basin. This particular latitude is chosen as it lies on a neutral point between regions of wind-induced upwelling and downwelling.

Another quantity to be considered is the non-dimensional poleward heat flux as defined in (4.2). The third quantity is a measure of the strength of the thermohaline circulation in terms of the net mass transport of the meridional cell. To give a clearer description of the thermohaline circulation the continuity equation (2.25) is integrated with respect to x.

$$\int_0^{\frac{1}{2}} \left[\left(\frac{v}{m}\right)_y + \left(\frac{w}{m^2}\right)_z \right] dx = 0. \qquad (5.1)$$

Relation (5.1) permits the total transport in the vertical-meridional plane to be specified by a transport stream function, where

$$\Phi_y = \int_0^{\frac{1}{2}} \frac{w}{m^2}\, dx, \qquad (5.2)$$

and

$$\Phi_z = -\int_0^{\frac{1}{2}} \frac{v}{m}\, dx. \qquad (5.3)$$

The patterns of Fig. 16a, b and c correspond to the final solutions of cases I, IV and V, respectively. The patterns of the total transport stream function in the meridional plane show the effect of a wind stress at the upper surface. The common feature of all three solutions is a dominant counterclockwise cell. A narrow branch carries surface water northward, and a relatively narrow branch descends near the northern wall. The contrast between the limited areas of sinking and the broad areas of rising motion is in good qualitative agreement with observational studies. Note the gradual development of a much smaller, independent counterclockwise cell near the surface in the tropics as the wind effect becomes more important.

This feature in Fig. 16*c* is associated with the northward Ekman drift induced in the region of easterlies. It would be of great interest to determine if this predicted feature can be detected in water mass data for the tropical Atlantic.

The maximum value of Φ is a measure of the mass transport of any given branch of the thermohaline circulation cell. To convert the nondimensional values given in Fig. 16 we note that

$$\Phi' = \varrho_0 V^* a d \Phi. \qquad (5.4)$$

Following the notation of Section 2, Φ is the dimensionless form, and Φ' the dimensional form.

In Table 5.1 the thermocline depth, heat transport and the strength of the thermohaline circulation are all given for the final solution of the 8 different cases given in Table 4.2. The values of ξ in Table 5.1 indicate that the temperature falls to $\frac{1}{2}$ its surface value at 20° N at approximately one scale depth below the surface. The minimum penetration occurs in Case II for which the lateral mixing has a very large value.

Nondimensional heat transport is 0.3 for most cases. Values of HT^* given in Table 4.1 may be used to interpret the results. The anomalously large heat transport for Case II is probably due to the 30 % contribution of lateral mixing to heat flux in this solution. On the other hand, the high value in Case VIII is directly related to a more vigorous thermohaline circulation, apparent in the value of Φ_{max}. The much lower rotational constraint (less than Case I by a factor of 100) permits a more direct response in the flow pattern to the north-south heating gradient. It is a surprising result that the difference in the thermohaline circulation is not greater.

Note that the introduction of wind has no apparent effect on the heat transport, and the strength of the meridional circulation. The Ekman drift below the westerly winds at middle latitudes tends to inhibit the northward movement of surface water that occurs in the purely thermal case. The effect on the heat transport is offset, however, by the stronger gyre that forms when wind is present. As applied to the real ocean this very interesting result based on the present set of calculations must be considered tentative until supplementary calculations can be carried out in higher ranges of Pé and Re.

For making a comparison with North Atlantic data it can be seen from Table 5.1 that the

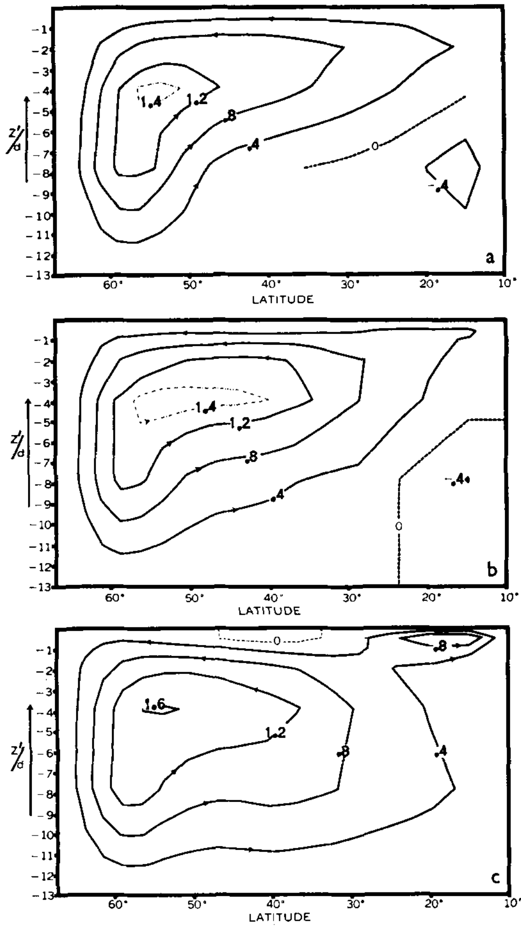

FIG. 16. Stream lines for the total mass transport in the vertical-meridional plane. *a*, Case I (no wind); *b*, Case IV (moderate wind); *c*, Case V (large wind).

TABLE 5.1. *ξ, HT/HT^*, and Φ_{max} corresponding to the final solutions.*

Case	I	II	III	IV	V	VI	VII	VIII
ξ	1.2	0.7	0.9	1.2	1.2	1.2	1.2	1.2
HT/HT^*	0.3	0.6	0.3	0.3	0.3	0.2	0.3	0.7
Φ_{max}	1.4	1.0	1.2	1.5	1.6	1.2	1.8	2.5

Fig. 17 a

Fig. 17 b

Fig. 17 c

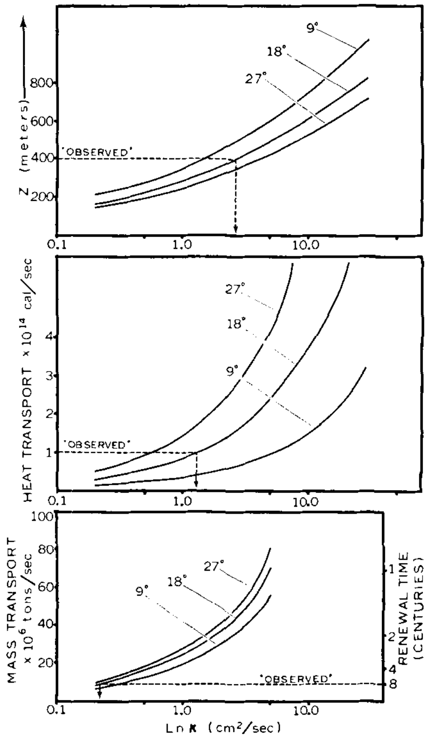

FIG. 17. (a) Depth at which the temperature falls to ½ the surface value at 20° N, (b) Total poleward heat transport, (c) Transport of thermohaline circulation and renewal time. The curves are based on the results for Case I.

results of Case I are fairly representative. Figure 17*a*, *b*, and *c* is intended to display the results of Case I in a form which allows a geophysical interpretation. The depth of the thermocline, ξ, the heat transport and the strength of the meridional circulation are plotted as functions of the vertical diffusion, $\varkappa$, and the temperature difference, $\Delta\vartheta^*$, which is impressed through the surface boundary condition. Other constants which specify the equation of state and dimensions of the basin have the same fixed values that are given in section 3.

In Fig. 17*a* the horizontal dashed line labled "observed" is based on temperature observations made at 16° N and 24° N in the Atlantic during the IGY (FUGLISTER, 1960). An average between these latitudes indicates that the temperature falls to ½ its surface value at 400 meters in the center of the ocean basin. Allowing for the effect of salinity, an apparent temperature difference, $\Delta\vartheta^*$, of 18° corresponds most closely to the North Atlantic. A vertical line drawn from the intersection point of the "observed" depth and the 18° line indicates that the corresponding value of the vertical diffusion, $\varkappa$, is about $2\frac{1}{2}$ cm²/s.

Since the North Atlantic is in free communication with the rest of the world ocean, there is a complication in finding an appropriate "observed" value of heat transport. In Fig. 18 poleward heat transport estimates based on the heat balance computations of ALBRECHT (1960), BUDYKO (1956) and SVERDRUP (1957) are denoted by *A*, *B* and *S*, respectively. Note that all three curves indicate a substantial amount of heat transfer from the South to the North Atlantic. Such a transport appears to be entirely reasonable in view of independent considerations based on water mass analysis. In order to make a comparison with the present calculations for a closed basin the heat transport estimates in Fig. 18 at 30° N are reduced by an amount equal to the heat flux at the equator. The observed level of poleward heat flux in Fig. 17*b* is set equal to 10^{14} cal/s based on a rough average of the different curves in Fig. 18.

C^{14} measurements indicate that the North Atlantic deep water has an apparent age of 8–10 centuries (BROEKER *et al.*, 1960). One way to interpret the evidence is that the apparent age corresponds to the average renewal time of the basin. To make a comparison with the model a renewal time in Fig. 17*c* is computed by dividing the total mass of water contained in a basin 5 kilometers deep by the mass transport of the thermohaline circulation. For example an overturning time of 8 centuries corresponds to 9 million tons/s transport in the thermohaline circulation. The value of the vertical

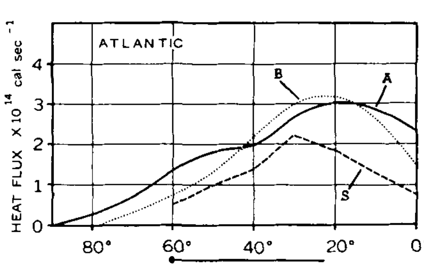

FIG. 18. Estimates of the actual poleward transport of heat by ocean currents in the North Atlantic. *A*, *B* and *S* indicate the curves based on the heat balance calculations of ALBRECHT (1960), BUDYKO (1956), and SVERDRUP (1957).

diffusion coefficient, $\varkappa$, corresponding to the "observed" renewal time based on C^{14} data is 0.2 cm^2/s, considerably less than that indicated by the thermocline depth and heat transport.

Independent empirical estimates based on water mass analysis indicate that $\varkappa$ should be of the order of unity in cgs units. Within an order of magnitude range centered on unity $\varkappa$ may be considered a constant at our disposal. Examination of Fig. 17 shows, that no single choice will simultaneously allow the model to fit "observed" values of thermocline thickness, heat transport and renewal time. For example, a choice of exactly unity for $\varkappa$ would fit the heat transport, but would produce too thin a thermocline and a renewal time of only two centuries. A similar conclusion has been reached previously in a study of the abyssal circulation of the world ocean by STOMMEL & ARONS (1960). Based on a very simplified dynamical model of the thermocline these authors found that the renewal time suggested by the observed penetration of the thermocline is considerably less than that indicated by C^{14} evidence. In future numerical calculations it would be of great interest to carry along the field of C^{14} as an extra variable, since part of the difficulty may be a misinterpretation of the relation between the radiochemical data and the circulation pattern.

Summary and conclusions

In order to investigate the time-averaged general circulation of the ocean a mathematical model is formulated based on the hydrostatic assumption and the Boussinesq approximation with respect to density. It differs from the thermocline model of ROBINSON & STOMMEL (1959) in that it includes lateral mixing of heat and momentum as a dissipative mechanism, as well as the nonlinear terms in the momentum equations. For stable stratification the vertical mixing coefficient for heat is a constant as in the thermocline theories, but for unstable stratification it becomes infinite.

In a test calculation the final solution of the numerical model is compared with a solution based on the similarity theory of ROBINSON & WELANDER (1963). Open lateral boundary conditions are chosen for the numerical calculation to exactly correspond to the theory. The Robinson and Welander model is geostrophic and the numerical model uses more complete equations, but this difference should not be important for the interior flow regime considered. An initial value calculation starting with horizontally uniform stratification converges to a final steady solution in satisfactory agreement with the similarity theory.

A dimensional analysis indicates that the solution of the model for a closed basin of planetary scale depends on 5 different parameters. A series of 8 initial value calculations, in which the system is allowed to approach an equilibrium, are considered. Each parameter is varied in turn, and the results are compared to a reference case for which the parameters are chosen to correspond as closely as possible to the geophysical range, but with wind stress absent. The equilibrium solution for the reference case reproduces the principal features of the purely thermohaline circulation predicted by STOMMEL (1958, p. 159). A shallow anticyclonic circulation is present near the surface extending over the entire basin. In the deeper water a much weaker cyclonic gyre is present. Western intensification is evident in both the upper and lower gyres. Some sinking occurs over wide areas in the northern part of the basin, but maximum vertical velocities occur in a concentrated area of sinking near the northeast corner of the basin.

The purely thermal circulation of the reference case differs in an important way from that observed in the North Atlantic and North Pacific in that the subarctic gyre is completely missing. In addition, the southward flowing branch of the anticyclonic gyre, which fills up the entire basin in the computed solution, consists of a weak current that is nearly uniform throughout the depth of the thermocline.

A test of the effect of changing the Rossby number, while keeping all other parameters constant, indicates that the geostrophic constraint is so great in the geophysical range, that the principal features of the circulation are retained even for a decrease of the effective rotation rate by a factor of 100. The important differences in the equilibrium solutions are an increase in width of the western boundary current, and an intensification of overturning in the vertical-meridional plane.

Another set of calculations allows a comparison of a thermal circulation, in which the ratio of the scale depth of the thermocline to the total depth is 13, to a case in which this ratio is 130. The results indicate a very similar temperature structure near the surface in both cases, and the poleward heat transfer by ocean currents is nearly the same.

The effect of a wind stress pattern corresponding to easterlies in the tropics and westerlies in middle latitudes produces striking changes in the patterns. The single, large anticyclonic gyre of the reference solution is broken down into a subtropical and subarctic gyre. The boundary between these two gyres coincides with the latitude of maximum westerly wind stress. In the center of the subtropical gyre the isothermal surfaces slope upwards to the east. Unlike the pure thermal case, the velocity in the southward moving branch of the subtropical gyre increases upwards with a pronounced maximum at the surface. Both these tendencies bring the patterns of the solutions into much closer agreement with observations.

The advection of temperature leads to the formation of an intense north-south gradient at the point along the western wall where the southward moving boundary current associated with the subarctic gyre meets the northward moving part of the western boundary current. On the eastern side of the basin at the same latitude the north-south temperature gradient is a minimum where the westerly drift splits and moves to the north and the south.

An examination of the results indicate that important integral properties of the solutions such as the total poleward heat transport and the turnover rate of the thermohaline circulation are remarkably insensitive to small changes in the basic independent parameters. When representative values of thermocline penetration and heat transport in the model calculations are compared to North Atlantic data, it is found that a fairly good match can be achieved by a choice of vertical mixing coefficient, $\varkappa$, to be 1 cm^2/s. A discrepancy occurs with respect to the renewal time of deep water. C^{14} data indicate that the apparent age of North Atlantic deep water is 8 to 10 centuries, but a value of $\varkappa$ of 1 cm^2/s implies a renewal time of less than 2 centuries in the present model.

Although many important effects, such as bottom friction, irregular bottom topography, and nonlinear terms in the equation of state have been omitted in the present model, there are no inherent difficulties to systematically incorporating them in future studies. A more serious defect is the implicit treatment of the interaction of smaller scale, transient disturbances with the time-averaged flow. Actual measurements support the vertical diffusion mechanism of the present model, although little is known of the actual scales of motion involved. On the other hand, the one available series of observations of the horizontal eddy transport of momentum (WEBSTER, 1965) indicates that over the continental shelf disturbances in the Gulf Stream actually concentrate momentum in a jet rather than diffuse it. The quantitative significance of Webster's results, based on surface measurements, for the maintenance of the Gulf Stream is unknown, but they indicate that at least locally the turbulent viscosity assumption for horizontal motion is completely inaccurate. Future studies should be directed toward much more detailed calculations in which the larger scale transient motions can be treated explicitly, thus eliminating to a large extent the dependence of the model on any particular hypothesis concerning the horizontal eddy transport of heat, salinity and momentum.

Acknowledgements

The authors are very grateful to Sol Hellerman, Martha Jackson and Joyce Harrison for very able assistance in preparing the drawings, typing and proofreading the manuscript. Many of the ideas for the numerical scheme of the computation were received from Douglas K. Lilly, Yoshio Kurihara and Kikuro Miyakoda. Comments on two earlier versions of the manuscript by Henry Stommel, George Veronis and Pierre Welander have been very helpful. The test calculation of Appendix A is based on a suggestion by Robert Blandford. Finally, a most important factor has been the sustained interest and support of Joseph Smagorinsky and Syukuro Manabe.

APPENDIX A

Comparison with a thermocline similarity solution

Since the results obtained by ROBINSON & WELANDER (1963) are used to test the present model, their theory will be briefly reviewed. In a single formulation Robinson & Welander are able to combine the principal elements of two previous studies of the thermocline by ROBINSON & STOMMEL (1959) and WELANDER (1959). Their theory is for the steady flow in a subtropical ocean gyre away from strong boundary currents. The thermocline is treated as a thermal boundary layer. While the horizontal dependence is taken into account by a similarity transformation, the vertical dependence is calculated directly from the theory.

The mathematical model of the thermocline used by Robinson & Welander is essentially that given by (2.21)–(2.25) assuming; (1) a steady state, (2) zero Rossby number, (3) infinite Reynolds' number and Péclèt number. A potential function is defined as

$$M = \int_{-\infty}^{z} \int_{-\infty}^{z'} \vartheta dz_1 dz_2 + c(x, y), \qquad (A.1)$$

where z_1 and z_2 are dummy variables, and c is an arbitrary function independent of z. Substituting (A.1) into the simplified form of the model,

$$-M_{zzzz} - \frac{m^2}{n} M_{yz} M_{zzx} + \frac{m^2}{n} M_{xz} M_{zzy} + \frac{1}{n^2} M_x M_{zzz} = 0. \qquad (A.2)$$

The similarity solution is based on a new variable, η, defined as

$$\eta = n^a [x + E(y)]^b z \mu^{1/3}. \qquad (A.3)$$

a and b are constants, and E is a function of y only. μ is a new constant not in previous formulations. It is needed here because we wish to define a dimensionless temperature in such a way that it is always equal to unity at a specified latitude. Following a convenient suggestion by BLANDFORD (1965), the constant b is defined so that $(x+E)^b$ and $-(x+E)^{3b+1}$ are always positive if $(x+E) < 1.5$. The solution is then

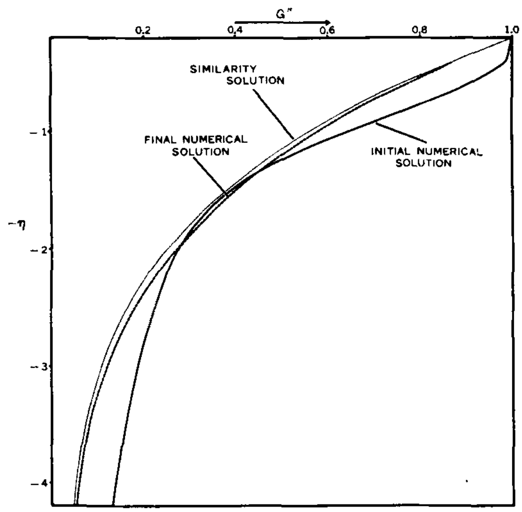

FIG. A.1. A sketch of the Function G'' as a function of the transformed depth, η. "Initial" and "final indicate the average value of $\bar{G}''$ over the entire region considered at the beginning and end of the computation. "Similarity solution" indicates the ROBINSON & WELANDER theory (1963).

$$M = \frac{\mu}{2} n^{a+2} (x+E)^{b+1} G(\eta). \qquad (A.4)$$

Expressions may be obtained for ϑ and w, where primes denote differentiation with respect to η.

$$\vartheta = M_{zz} = -\frac{\mu}{2} n^{3a+2} (x+E)^{3b+1} G'', \qquad (A.5)$$

$$w = -\frac{\mu}{2} n^a (x+E)^b [(b+1) G + b\eta G'']. \qquad (A.6)$$

By substituting (A.4) into (A.2) an ordinary, fourth order, nonlinear differential equation is obtained for G. For purposes of testing the numerical model the solution is obtained for the special case in which a is equal to -1 and b is equal $-\frac{1}{3}$, corresponding to a case in which the temperature specified at the surface is inversely proportional to the sine of latitude and independent of longitude. A sketch of the solution is shown in Fig. A.1.

The test calculation is carried out for a region exactly equivalent to that of the basin discussed in the main body of the paper. In this case, however, the region is bounded by a wall only

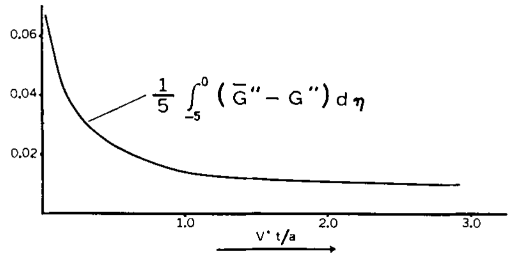

Fig. A.2. Difference between the calculated value of $\bar{G}''$ from the numerical model and G'' from theory as a function of time.

on the east side. The theory requires inflow along the north boundary, and outflow along the western and southern boundaries. The lateral boundary conditions of the test calculation are:

$$\vartheta = \vartheta^*, \quad u_x = v_x = 0, \quad x = 0 \tag{A.7}$$

$$\vartheta = 0, \quad u_x = v_x = 0, \quad x = 1.5 \tag{A.8}$$

$$\vartheta = \vartheta^*, \quad u_y = v_y = 0, \quad y = y_1 \tag{A.9}$$

$$\vartheta = \vartheta^*, \quad u_y = v_{yy} = 0, \quad y = y_2 \tag{A.10}$$

Asterisks denote the temperature distribution given by the Robinson–Welander theory. Since the flow is very nearly geostrophic, fixing the temperature at the boundaries is nearly equivalent to specifying the inflow and outflow. For this reason the weak conditions on the normal velocity components given in (A.7), (A.9) and (A.10) are sufficient. The boundary conditions at the top and bottom boundaries are exactly the same as given by (2.14) and (2.15), except for the different dependence on latitude of the temperature specified at the top boundary.

The numerical calculations are carried out for a regular 17×17 grid. The non-dimensional parameters have the same values as in Case I except that H/d is 130 instead of 13. This large value of H/d is chosen to correspond to the

TABLE A.1. *The horizontally uniform, initial temperature distribution used in the test calculation.*

Z'/d	0.3	0.6	1.3	2.6	5.2	10.4
ϑ	0.39	0.17	0.10	0.03	0.01	0.00

condition of infinite depth of the similarity theory. The temperature inside the lateral boundaries is initially horizontally uniform below the surface. The distribution with respect to depth is given in Table A.1.

To obtain a simple measure of the convergence of the numerical calculation a new quantity $\bar{G}''$ is defined. If one makes use of the expression for temperature given in (A.5), it is possible to define the following integral,

$$\bar{G}''(\eta) = \frac{-2}{\mu \times \text{Area}} \int_0^{1.5} \int_{y_1}^{y_2} n m^{-2} \vartheta(\eta)\, dy\, dx, \tag{A.11}$$

where
$$\text{Area} = \int_0^{1.5} \int_{y_1}^{y_2} m^{-2} dy\, dx. \tag{A.12}$$

$\bar{G}''$ represents a weighted mean of the temperature on surfaces of constant η over the entire region of the numerical calculation. The initial and final distributions of $\bar{G}''$ in the numerical calculation are shown in Fig. A.1. Since the temperature specified at the surface varies as the inverse sine of the latitude, convective adjustment rapidly alters the horizontally uniform temperature pattern of the initial conditions. The curve marked "initial" in Fig. A.1 is at the beginning of the computation just after this convective adjustment has taken place.

In Fig. A.2 the difference between $\bar{G}''$ and G'' from the Robinson & Welander theory averaged over the interval $0 > \eta > -5$ is plotted as a function of time. In the course of the numerical integration this average converges to less than 0.01. In Fig. A.3 an east-west and a north-south temperature section are shown which allow a comparison between the numerical results and the similarity solution. Some effects of lateral mixing and possible truncation error are evident at the eastern wall. The calculated thermocline depth in the center of the basin is 10 % too deep.

In a comparison of solutions for cases I, IV, and V in section 4, a discrepancy is noted between the results of the present calculations and a previous study of the thermocline by ROBINSON & STOMMEL (1959). The point of interest is whether the slope upwards to the east of the isotherms throughout the depth of the thermocline is produced by a thermal circulation alone, or whether it is essential for the thermal circulation to be modified by wind at the surface. The test calculation given in

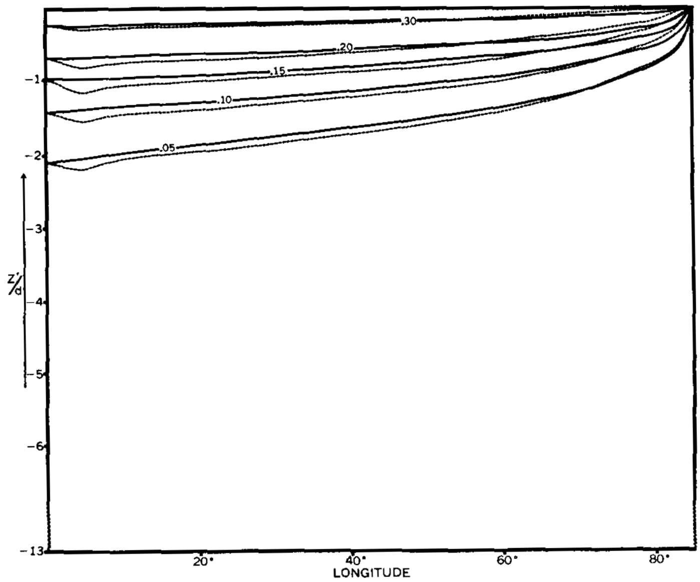

Fig. A.3*a*

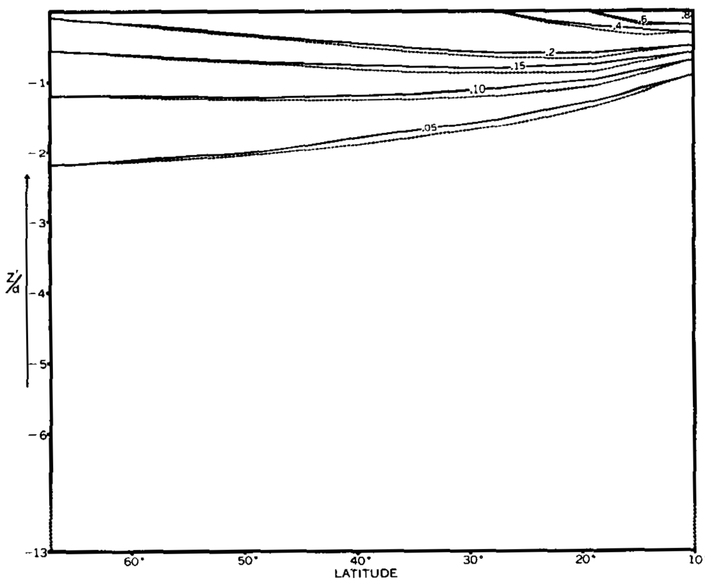

Fig. A.3*b*

Fig. A.3 (*a*) An east-west cross-section and (*b*) a north-south section of the final temperature pattern of the test calculation. Solid and dashed lines indicate theory and numerical results, respectively. Note the shallow penetration of the thermocline as compared to Figs. 7 and 11.

this appendix demonstrates that a satisfactory correspondence with the more exact version of the thermocline theory given by ROBINSON & WELANDER (1963) can be obtained with the numerical model. This indicates that differences in lateral boundary conditions are the primary source of the discrepancy with the ROBINSON & STOMMEL (1959) study noted above.

APPENDIX B

Numerical procedure for calculating the thermal circulation

In setting up a procedure for the numerical integration of the model, it is first convenient to put the continuous equations in a more convenient form. Differentiating (2.1) and (2.2) with respect to z, and substituting the hydrostatic relation,

$$[\dot{u} - n(2\Omega + um/a)v - F^x]_z = -mg\alpha\vartheta_x, \quad (B.1)$$

$$[\dot{v} + n(2\Omega + um/a)u - F^y]_z = -mg\alpha\vartheta_y. \quad (B.2)$$

Since ω is zero at the surface, it is possible to define a stream function for the vertically integrated flow.

$$\psi_x = \int_{-H}^{0} \varrho_0 \frac{v}{m} dz, \quad \psi_y = -\int_{-H}^{0} \varrho_0 \frac{u}{m} dz. \quad (B.3)$$

If both (2.1) and (2.2) are divided by m, and (2.1) is differentiated with respect to y, and subtracted from (2.2) differentiated with respect to x,

$$\nabla^2 \psi_t = -\frac{2\Omega}{m^2 a}\psi_x + \int_{-H}^{0} \varrho_0 \left\{ \left[\left(\dot{u} - u_t - \frac{uvmn}{a} - F^x \right) \Big/ m \right]_y - \left[\left(\dot{v} - v_t + \frac{uunm}{a} - F^y \right) \Big/ m \right]_x \right\} dz. \quad (B.4)$$

In contrast to the main body of the paper dimensional quantities are not primed.

The finite difference equations make use of (B.1) and (B.2) to find the deviation of the horizontal velocity components from a vertical average (the internal mode). The vertically averaged component may then be calculated from (B.4).

Let the continuous variables x, y, t and z be replaced by the discrete variables i, j, n and k where

$$\left.\begin{array}{ll} x = (i - \frac{1}{2})\Delta s & i = 1, 2, 3 \ldots I \\ y = (j - \frac{1}{2})\Delta s & j = 1, 2, 3 \ldots J \\ t = n\Delta t & n = 1, 2, 3 \ldots N \end{array}\right\} \quad (B.5)$$

The vertical spacing of the numerical net is chosen to give the greatest resolution near the surface.

$$\left.\begin{array}{l} z_k = -1.3d \times 2^{k-3}, \quad k = 1, 2, 3 \ldots K, \\ \Delta_k z = z_{k-\frac{1}{2}} - z_{k+\frac{1}{2}}, \\ z_k = (z_{k-\frac{1}{2}} + z_{k+\frac{1}{2}})/2, \quad k = \frac{3}{2}, \frac{5}{2} \ldots, \\ z_{\frac{1}{2}} = 0, \quad z_{K+\frac{1}{2}} = -H. \end{array}\right\} \quad (B.6)$$

Most of the computations are carried out for a net consisting of 17×17 interior points with 6 levels in the vertical. The spacing varies with latitude, but for a basin of planetary scale, Δs would be roughly 300 kilometers.

To provide a more concise notation for setting down the finite difference equations, we define

$$\delta_x(\ ) = [(\ )_{i+\frac{1}{2},j} - (\ )_{i-\frac{1}{2},j}]/\Delta s \quad (B.7)$$

and

$$\overline{(\ )} = [(\ )^x_{i+\frac{1}{2},j} + (\ )_{i-\frac{1}{2},j}]/2. \quad (B.8)$$

Note that

$$\delta_x \overline{(\ )}^x = [(\ )_{i+1,j} - (\ )_{i-1,j}]/2\Delta s. \quad (B.9)$$

The three variables u, v, and ϑ are defined at integral values of i, j and k.

The continuity equation is given as

$$m^2 \delta_x \left(\frac{\bar{u}^{xyy}}{m} \right) + m^2 \delta_y \left(\frac{\bar{v}^{yxx}}{m} \right) + \delta_z w = 0. \quad (B.10)$$

It is convenient to combine the continuity equation with the advective terms in the following operator,

$$D\mu = m^2 \delta_x \left(\frac{\bar{u}^{xyy}}{m} \bar{\mu}^x \right) + m^2 \delta_y \left(\frac{\bar{v}^{yxx}}{m} \bar{\mu}^y \right) + \delta_z w \bar{\mu}^z, \quad (B.11)$$

where μ is some scalar quantity defined at integral values of i, j and k. Note that w is defined at integral values of i and j, but in the Z-direction at $k = \frac{1}{2}, \frac{3}{2} \ldots$ etc.

With this notation the continuous equation

$$\dot{\vartheta} = Q$$

may be written

$$(\vartheta^{n+1} - \vartheta^n)/\Delta t = \tfrac{3}{2}(-D\vartheta + Q)^n - \tfrac{1}{2}(-D\vartheta + Q)^{n-1} \quad (B.12)$$

and

$$Q = \left[\frac{\varkappa}{|\delta|}\delta_z\delta_z + m^2 A_H(\delta_x\delta_x + \delta_y\delta_y)\right]\vartheta. \quad \text{(B.13)}$$

This method of forward differencing has been discussed by LILLY (1965). It has the advantage of eliminating the computational mode with only a slight decrease in accuracy.

The two horizontal velocity components are calculated in a similar manner.

$$\delta_z(u^{n+1} - u^n)/\Delta t - 2\Omega n\delta_z[\gamma v^{n+1} + (1-\gamma)v^n] = \tfrac{3}{2}G^n - \tfrac{1}{2}G^{n-1}, \quad \text{(B.14)}$$

$$\delta_z(v^{n+1} - v^n)/\Delta t + 2\Omega n\delta_z[\gamma u^{n+1} + (1-\gamma)u^n] = \tfrac{3}{2}J^n - \tfrac{1}{2}J^{n-1}, \quad \text{(B.15)}$$

where

$$G = -g\alpha m\delta_x\bar{\vartheta}^{xyyz} + \delta_z\left(-Du + \frac{nmuv}{a} + F^x\right) \quad \text{(B.16)}$$

and

$$J = -g\alpha m\delta_y\bar{\vartheta}^{yxxz} + \delta_z\left(-Dv - \frac{nmuu}{a} + F^y\right) \quad \text{(B.17)}$$

and

$$F^x = \varkappa\delta_z\delta_z u + m^2 A_M(\delta_x\delta_x + \delta_y\delta_y)u, \quad \text{(B.18)}$$

$$F^y = \varkappa\delta_z\delta_z v + m^2 A_M(\delta_x\delta_x + \delta_y\delta_y)v. \quad \text{(B.19)}$$

The constant, γ, which appears in (B.14) and (B.15) controls the weighting of the coriolis term between the $n+1$ time step and the previous step. γ equal to $\tfrac{3}{4}$ gave the most satisfactory results for the long time steps (order of one day) used in the present calculations.

Equations (B.14) and (B.15) form two simultaneous equations which may be solved to find $\delta_z u^{n+1}$ and $\delta_z v^{n+1}$, since the other terms depend on information calculated at previous time steps. To find new values of the transport stream function,

$$(\delta_x\delta_x + \delta_y\delta_y)(\psi^{n+1} - \psi^n)/\Delta t = \tfrac{3}{2}E^n - \tfrac{1}{2}E^{n-1}, \quad \text{(B.20)}$$

where

$$E = -\frac{2\Omega}{am^2}\delta_x\bar{\psi}^x + A_M m^2(\delta_x\delta_x + \delta_y\delta_y)^2\psi - \sum_{k=1}^{K}\varrho_0\left\{\delta_x\left[\overline{\left(Dv - \frac{nmuu}{a} + \varkappa\delta_z\delta_z v\right)\Big/m}\right]^y - \delta_y\left[\overline{\left(Du + \frac{mnuv}{a} + \varkappa\delta_z\delta_z u\right)\Big/m}\right]^x\right\}\Delta_k z. \quad \text{(B.21)}$$

Equations (B.20) and (B.21) are not completely equivalent to (B.4), since certain terms depending on the latitudinal variation of m are not included.

The stream function is calculated only at midpoints with the coordinates $i+\tfrac{1}{2}$ and $j+\tfrac{1}{2}$. To find the vertically averaged component of velocity,

$$\int_{-H}^{0}\varrho_0 u\,dz = -\delta_y\bar{\psi}^x, \quad \text{(B.22)}$$

$$\int_{-H}^{0}\varrho_0 v\,dz = \delta_x\bar{\psi}^y. \quad \text{(B.23)}$$

The actual values of velocity at each level are obtained by integrating $\delta_z u^{n+1}$ and $\delta_z v^{n+1}$ with respect to depth. The constant of integration is obtained from (B.22) and (B.23).

In the case of the uniform grid of 17×17 points in the horizontal plane and 6 levels in the vertical, each time step requires about 6 seconds of calculation on an IBM 7030 ("Stretch"). Further details regarding the numerical formulation of boundary conditions and the use of an irregular grid with extra resolution at the western boundary have been written up in the form of a memorandum. This memorandum may be obtained on request from the Geophysical Fluid Dynamics Laboratory, Environmental Science Services Administration, Washington, 25, D.C., U.S.A.

REFERENCES

ALBRECHT, F., 1960, Jahreskarten des Wärme- und Wasserhaushaltes der Ozeane. *Ber. Deut. Wetterdienstes*, **66**, Bd. 9, 19 pp.

ARAKAWA, A., 1963, Computation design for long-term numerical integrations of the equations for atmospheric motion. Paper presented at the 44th Annual Meeting, A.G.U., Washington, April 1963.

BLANDFORD, R., 1965, Notes on the theory of the thermocline. *J. Mar. Res.*, **23**, pp. 18–29.

BROEKER, W. C., GERARD, R., EWING, M., and HEEZEN, B. C., 1960, Natural radiocarbon in the Atlantic Ocean. *J. Geophys. Res.*, **65**, 2903–2931.

BRYAN, K., 1963, A numerical investigation of a non-linear model of a wind-driven ocean. *J. Atmos. Science*, **20**, pp. 594–606.

BRYAN, K., 1966, A scheme for numerical integration of the equations of motion on an irregular grid free of nonlinear instability. *Mon. Wea. Rev.*, U.S.W.B. *94*, pp. 39–40.

BUDYKO, M. I., 1956, *The Heat Balance of the Earth's Surface.* Translated by N. A. STEPANOVA, 1958, WASHINGTON, D.C., U.S. Department of Commerce, 259 pp.

FOFONOFF, N. P., 1962, Dynamics of ocean currents. *The Sea*, Vol. I, M. N. Hills Editor, N.Y., London, J. Wiley.

FUGLISTER, F. C., 1960, *Atlantic Ocean Atlas.* Woods Hole Oceanographic Inst. Atlas, Ser. 1, 209 pp.

GORMATYUK, YU. K., and SARKISYAN, A. S., 1965, Results of four-level model calculations of North Atlantic currents. Izv. Akad. Nauk (U.S.S.R.) *Atmos. and Oceanic Physics*, **1**, pp. 313–326.

LILLY, D. K., 1965, On the computational stability of numerical solutions of time-dependent, non-linear geophysical fluid dynamics problems. *Mon. Wea. Rev.*, **93**, pp. 11–25.

LINEYKIN, P. S., 1955, On the determination of the thickness of the baroclinic layer of the sea. *Dokl. Akad. Nauk* USSR, **101**, pp. 461–464.

LINEYKIN, P. S., 1962, Some new research on the dynamics of ocean currents. *20th Anniversary Vol.*, Tokyo, Ocean. Soc. Jap., pp. 448–457.

ROBINSON, A. R., 1960, The general thermal circulation in equatorial regions. *Deep-Sea Res.*, **6**, pp. 311–317.

ROBINSON, A. R., and STOMMEL, H., 1959, The oceanic thermocline and the associated thermohaline circulation. *Tellus*, **11**, pp. 295–308.

ROBINSON, A. R., and WELANDER, P., 1963, Thermal circulation on a rotating sphere: with application to the oceanic thermocline. *J. Mar. Res.*, **21**, pp. 25–38.

SARKISYAN, A. S., 1962, On the dynamics of the origin of wind currents in the baroclinic ocean. *Okeanologia*, **11: 3**, pp. 393–409.

SMAGORINSKY, J., 1963, General circulation experiments with the primitive equations. *Mon. Wea. Rev.*, U.S.W.B., **91**, pp. 99–164.

STOMMEL, H., 1958, *The Gulf Stream, a Physical and Dynamical Description.* Berkeley, Univ. Calif. Press, 157 pp., 2nd Edition, 1965.

STOMMEL, H. and ARONS, A. B., 1960, On the abyssal circulation of the world ocean—II, *Deep-Sea Res.*, **6**, pp. 217–233.

STOMMEL, H. and WEBSTER, J., 1962, Some properties of thermocline equations in a subtropical gyre. *J. Mar. Res.*, **20**, pp. 42–56.

SVERDRUP, H. U., 1947, Wind-driven currents in a baroclinic ocean; with application to the equatorial currents of the Eastern Pacific. *Proc. Natl. Acad. of Sci* (U.S.A.), **33**, pp. 318–326.

SVERDRUP, H. U., 1957, Oceanography. In *Handbuch der Physik*, **48**, Berlin, Springer-Verlag.

WEBSTER, F., 1965, Measurements of eddy fluxes of momentum in the surface layer of The Gulf Stream. *Tellus*, **17**, pp. 239–245.

WELANDER, P., 1959, An advective model of the ocean thermocline. *Tellus*, **11**, pp. 309–318.

WÜST, G., and DEFANT, A., 1936, Meteor 1925–1927. *Wissenschaftliche Ergebnisse*, Bd. **6**—Atlas (103 pls). Berlin, W. de Gruyter Co.

ИССЛЕДОВАНИЯ ОБЩЕЙ ЦИРКУЛЯЦИИ ОКЕАНА

Рассматривается бассейн постоянной глубины, ограниченный с боков по мередианам. Температура и ветровое напряжение на поверхности заданы как функции широты. Рассматривается модель аналогичная ранее использовавшимся моделям океанской термоклины, за исключением горизонтальной проекции уравнения количества движения, которая берется в почти полном виде.

Решение начальной задачи получено непосредственным численным интегрированием на электроновычислительной машине. Анализ размерностей показывает, что существенны 5 параметров. В 8-ми численных эксперементах исследуется геофизически существенная область изменений этих параметров. Вычисления при наличии и отсутствии ветра показали, что в крупномасштабной циркуляции имеется взаимодействие между термоклинной и ветровой компонентами. При отсутствии ветра всю поверхность бассейна занимает одно большое антициклонное вращение (по часовой стрелке) у западной границы имеется так же поверхностное течение, распространяющееся в высокие широты. Кроме того существует равномерное по вертикали, медленое течение в южном направлении между поверхностью и основанием термоклины. Меденное циклонное (против часовой стрелки) вращение существует ниже термоклины. При добавлении ветрового напряжения из максимума зональной циркуляции при 45° Cm образуется циклонное вращение в субарктических широтах. Несмотря на упрощенные граничные условия решение при наличии ветра воспроизводили многие детали наблюдаемого распределения плотности в северной Атлантике, в частности субтропическое вращение.

Количественное сравнение с данными северной Атлантики показывает что выбор коэффициента вертикальной диффузии $\varkappa$ равным 1 см²/сек дает близкое совпадение для глубины термоклины и оценок полного потока тепла на север.

Однако соответствующее время обновления для глубины воды заметно меньше, чем показывает анализ.